NTNU
Norwegian University of
Science and Technology

Spectral diagnostics and characterization of atopic dermatitis in children's health

A Hyperspectral Imaging System using an Acousto-Optic Tunable Filter

Morten Sikle Liland

Master of Science in Electronics
Submission date: February 2017
Supervisor: Lise Lyngsnes Randeberg, IES

Norwegian University of Science and Technology
Department of Electronic Systems

Project Description

Acousto-Optic tunable filters (AOTF) can be used for wavelength selection in multi- and hyperspectral imaging system. The main aim of this thesis is to test one such hyperspectral imaging system designed for imaging of human skin and to compare results from this system to spectra collected using a fiber-optic spectrometer. The system is intended for characterization of skin in children with atopic dermatitis, and pilot data from healthy skin and skin lesions in children with eczema should be collected using the AOTF-system and the fiber-optic spectrometer. The thesis should contain:

- A review of relevant literature and theoretical background for the thesis.
- A description of the AOTF-system
- A description of the tests performed on the system, and discussion of the achieved result. Relevant parameters include, but are not limited to, spatial and spectral resolution, depth of focus, aberration and artefacts, sensitivity and focus.
- A description of the pilot study carried out on atopic dermatitis and measurement on other relevant samples, together with an interpretation and discussion of these results.

Supervisor at the Department of Electronics and Telecommunications: Lise Lyngsnes Randeberg

Assignment given: 2016-09-11

Abstract

English

Hyperspectral imaging with high spectral and spatial resolution can be used to analyse material using spectroscopic methods. This technique can be applied to human tissue as a general purpose diagnostics tool and as an aid to medical personnel.

The light propagation in tissue can be modelled in numerous ways, among others is the radiative transport equation (RTE) and its approximation the diffusion approximation. The goal of this project is to assemble a camera system and use these models to characterise atopic dermatitis in children health. This will be done trough measurements with spectrometers and the assembled camera system and compare the two.

There was found a noticeable difference in the skin with and without atopic dermatitis, but quantitatively this has to be future explored. The proposed camera system was found not to be working, thought to be caused by internal reflection and miss alignment of optical components in the system.

These results can, in the future, be applied to a real-time diagnosis system to detect, and reduce the over and under treatment of atopic dermatitis.

Sammendrag

Bokmål

Hyperspektral avbildning med høy spektral og romlig oppløsning kan bli brukt for å analysere materialer ved hjelp av spektroskopiske metoder. Dette kan i først omgang bli brukt som et diagnose verktøy for medisinsk personell.

Lys propagasjonen i hud kan modelleres analytisk ved hjelp av likningen for strålingstransport, da denne er vanskelig å løse kan vi bruke diffusjonsmodellen til å finne en tilnærmet løsning. Målet med denne oppgaven er å sette sammen et kamerasystem og bruke disse modellen for å karakterisere atopisk dermatitt hos små barn. Dette vil bli gjort ved hjelp av målinger utført med spektrometer og det konstruerte kamerasystemet. Og disse vil bli sammenliknet.

Det ble funnet en sammenheng mellom hud med og uten atpoisk dermatitt, men dette må utforskes kvantitativt videre. Det foreslåtte kamerasystemet ble funnet å ikke fungere da det led av interne refleksjoner og at noen av de otiske elementene ikke kunne plasseres korrekt.

Disse resultatene kan i fremtiden bli brukt for å lage et system for å detektere, diagnostisere å redusere over- og underbehandlingen av atopisk dermatitt.

Preface

The work included in this thesis was carried out at the Department of Electronics and Telecommunication at the Norwegian University of Science and Technology in the fall of 2016 and spring 2017. As a final part of a Master of Science. The motivation behind this project is to develop a tool for skin diagnostic and assessment of atopic dermatitis based on a hyperspectral imaging system. The work presented here are only a pilot investigation of the optical properties of atopic dermatitis and will need more work before, hopefully, being used by doctors and patients.

I would like to give warm thanks to my supervisor Lise L. Randeberg, for all the help, support and opportunity to do this project. I also want to thank Asgeir Bjørgan for help with analysing data and answering questions I might have had. Thanks to Tore and Tore at the Tele-Engineering workshop, of which I would not have been able to bring the optical system out of the lab and into the field. Thanks to the children and their parents for letting me do measurements on them, and to the doctor attending for overlooking and bringing in the patients. And a small thanks to the rubber duck for help with debugging of the code. Thank you, Geir for helping me with suggestions based on your experience from your thesis, and for bear living with me for over half a decade! Special thanks to Anja for help with motivation, proofreading and being there for me. Last but not least I would thank my parents for the upbringing and making me interested in science and technology.

Morten S. Liland
February 2017, NTNU
Trondheim

Contents

List of Figures

List of Abbreviations and Acronyms

AOTF	Acousto-Optic Tunable filter
BIL	Band-interleved-by-line
BIP	Band-interleved-by-pixel
BSQ	Band-sequential
CCD	Charge Coupled Device
DN	Digital number
DP	Dead pixel
EMCCD	Electron Multiplying Charge Coupled Device
HP	Hot pixel
NP	Noisy pixel
RF	Radio Frequency
RTE	Radiative Transport Equation
UNP	Unphysical noisy pixels
UP	Un-linear pixel

Chapter 1

Introduction

Hyperspectral imaging is a technique where images are acquired in multiple narrow spectral bands instead of only three (red, green and blue) as in conventional photography. This technique has in recent times become a powerful tool for analysis in many different scientific fields and also in industry. Its applications range from aerial agricultural surveillance, trough food safety and forensics to space exploration and biomedical applications.

This thesis will focus on the use of reflectance spectroscopy to characterise and detect atopic dermatitis in children's health. This will be attempted done by use of a hyperspectral camera system described in [1]. This camera will be tested to measure its performance, and it will be compared to results gathered using a fiber-optic spectrometer. Pilot data of the lesion and normal skin has been gathered trough measurement on patients with atopic dermatitis in Oslo.

The structure of this thesis will be ass follow: first, a chapter introducing the theory of spectroscopy, the AOTF-imaging system and light propagation in the skin will be presented. Then the instrumentation setup will be explained before the protocol of how data was acquired is described. In chapter 5 results will be presented and discussed before, finally, in chapter 6 a conclusion and suggestions for future work will be presented.

Chapter 2

Theory

In the following sections theory of spectroscopy, spectroscopic imaging, optical systems and light transport in tissue are presented. This will include theory behind the hyperspectral imaging system built, the radiative transport equation and the diffusion approximation.

2.1 Spectroscopy

Spectroscopy is the study of the interaction of electromagnetic radiation and matter related to the dependence of wavelength and is often represented as a graph with intensity on the y-axis and wavelength (or frequency) on the x-axis. From this interaction, we can characterise, identify and analyse a broad range of matter, from the composition of stars to the structure of crystals [2][3].

2.2 Hyperspectral Imaging

As opposed to conventional photography, where each pixel contains colour intensities of three colour bands; red, green and blue, each pixel in a hyperspectral image comprises of colour intensities of numerous narrow bands similar spectroscopy. Depending on the width of these bands, and also the number of individual bands, the image is said to be multispectral, hyperspectral or ultraspectral [3]. As a note to the reader: this type of imaging is also called imaging spectroscopy in the literature.

2.2.1 Different type of HSI imaging

Images of high spectral resolution is typically called hyperspectral images while pictures of less spectral resolution are called multispectral images, where this limit goes depends on the acquisition range and the bandwidth of the individual images.

This limit is vague and not well defined in the literature, but most will agree that the difference will be dependent on the application and if an approximation of a continuous spectrum can be made or not. Where there are hundreds of such narrow bands it is called ultraspectral imaging to separate it from hyperspectral imaging [3]. There are different methods of acquiring spectroscopic images. The four primary methods will be presented briefly below [3].

Line scanning camera

First, we have the line scanning camera, also called a pushbroom scanner. This method requires the camera to scan over the scene, or the scene to move in front of the camera at a constant speed. This can pose a major issue if it is important to acquire the spectral image in a timely fashion. On the other hand, if the object or camera is moving at a constant or known speed this technique can be an excellent option e.g. when acquiring images from an aeroplane or satellite. The construction method of such a system can be to lay a colour gradient filter directly on a two-dimensional sensor and continuously record images while moving across the object. An alternative method is to use a prism to refract the light into different bands on the sensor as seen in Figure 2.1(b).

Spectral scanning

This technique, as opposed to line scanning, scans the image spectrally and can be used to capture the entire spatial image in one specified spectral band at a time. The use of this type of camera will be better when the object is only moving slightly because image registration will be easier to apply. To construct such a system, we need a method to filter the light into small spectral bands this can be done in multiple ways including the use of Acousto optic tunable filters (AOTF), liquid crystal tunable filters (LCTF) and filter wheels. The AOTF and LCTF are similar in operation while the filter wheel differs from the other two. The AOTF and LCTF utilise material properties of one stationary filter while the filter wheel uses multiple filters mounted on a wheel that can be mechanically moved in front of the camera to filter the light one band at a time. Acquisition principle can be seen from Figure 2.1(c)

Snapshot

The Snapshot method has fast acquisition time and will capture both the spatial and spectral information at the same time. Its limitation is the number of bands it can acquire. This limitation is due to the need for a large image sensor, or multiple sensors, in combination with optical components to get all the spectral data with a decent spatial resolution at the same time. For the principle of operation see Figure 2.1(d).

Whiskbroom

This might be the slowest approach as it requires the scanning of the object in both spatial directions, in effect capturing the spectrum of one pixel at a time. Also, the system is complex to make. From Figure 2.1(a) the principle of operation can be seen.

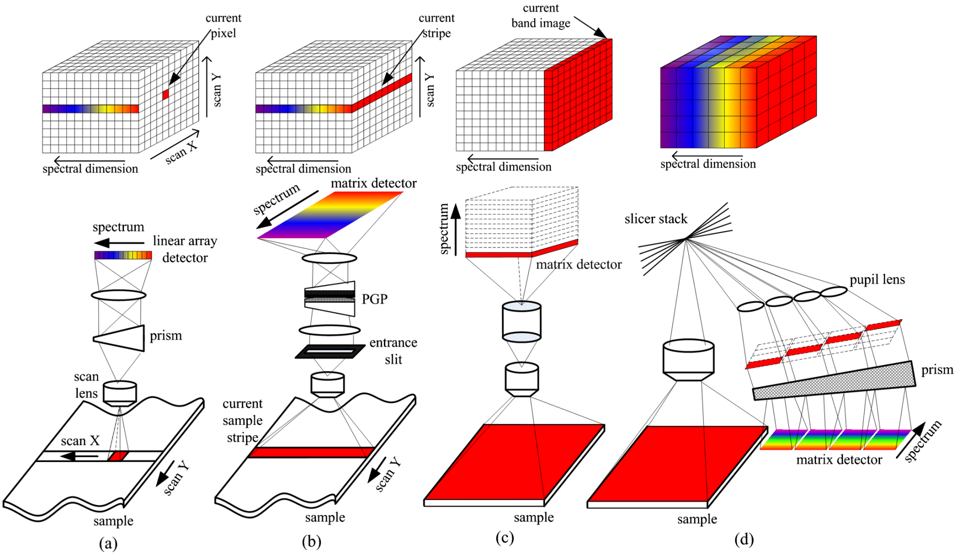

Figure 2.1: Different types of hyperspectral acquisition techniques. (a) Whiskbroom, (b) Pushbroom, (c) Staring, (d) Snapshot [3].

2.2.2 HSI data storage

The data gettered from a multi- or hyperspectral imaging system can be represented as a data-cube with two spatial axes and one spectral axis. When storing this HSI data cube to a single file, a problem occurs, how to write a three-dimensional image to a two-dimensional file? Depending on how we store them the read and write speed will be impacted. This has to be taken into consideration when writing code for the system. There are three main methods for storing HSI data cubes to files, these are the Band-Sequential (BSQ), Band-Interleaved-by-line (BIL), and Band-Interleaved-by-Pixel (BIP), here follows a short description of each, with pros and cons.

BSQ

This method of storing hyperspectral data cubes to files stores the image as multiple spatial images following each other with one wavelength for each spatial image this file layout can be seen from Figure 2.2. Using this method we can write directly to a file if we acquire one spatial image at a time. This format also gives easy access to the spatial information in the data cube but limits the access speed of spectral information because of the long distance between adjacent spectral images in memory.

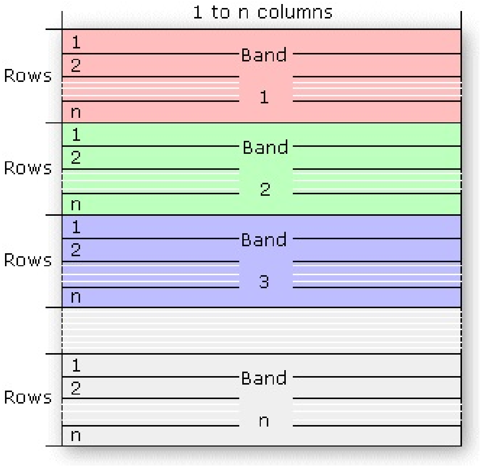

Figure 2.2: Showing the file layout of the BSQ interleave. The first row corresponds to the first spatial row of the image in the first band, then the second spatial row of the image in the first band follows. After the entire spatial picture of band one (red) is stored the next band (green) starts and so on. [4].

BIL

The Band-interleaved-by-line is well suited for line scanner cameras as the image is interleaved line by line as seen from Figure 2.3. This method is a compromise for accessing the spectral and spatial information in a timely fashion.

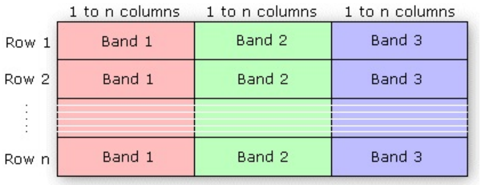

Figure 2.3: Showing the file layout of the BIL interleave. First row of the file contains the first row in the spatial image of band one(red), followed by the first row of the second band(green) and so on. The second line contains the second line of the spatial image for each band [4].

BIP

Band interleaved by pixel gives easy access to the spectral information for one pixel at a time as the data for each pixel is written band by band. Since the processing of hyperspectral images is often done on a pixel-by-pixel basis both this and the BIL format is more suitable than the BSQ format [5]. (See Figure 2.4).

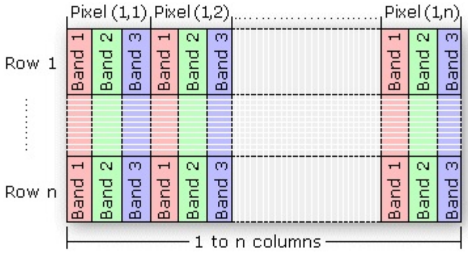

Figure 2.4: Showing the file layout of the BIP interleave. Here the first row in the file consists of the spectra for the first pixel on the first row of the spatial image followed by the spectra for the second pixel on the first row and so on. The second row contains the spectral information of the second row in the spatial image [4].

2.3 Imaging system

2.3.1 Camera

The Andor Zyla Camera used in this project is based on sCMOS technology. The reasoning behind the selection can be fond in [1] while the central principle of operation will be described in the following.

While other more established methods like Electron Multiplying charge coupled devices(EMCCD), exists. Which is based on CCD with an electron multiplying register to allow weak signals to be amplified before any read noise is added by the output amplifier, reducing the amount of noise produced. There have been decided to use the newer sCMOS technology, which has an integrated amplifier per pixel as shown in Figure 2.5.

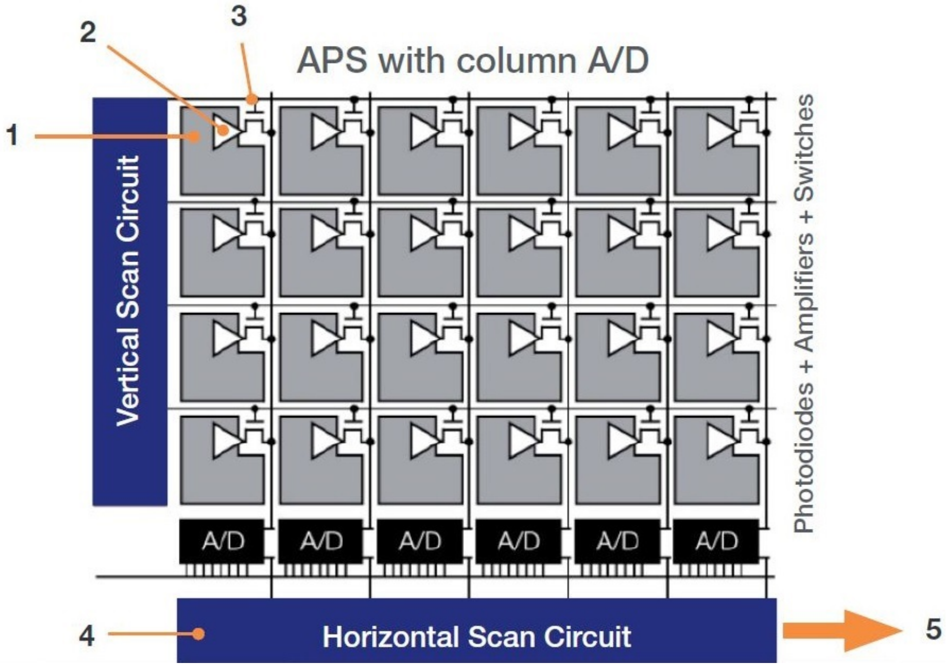

Figure 2.5: Image of a sCMOS array. 1. Photosensitive "pixel", 2. Built in amplifier for each pixel generating analogue signal, 3. Row select used to transfer the voltage to the column bus and into the analogue to digital converters(A/D), 4. Circuit to scan the horisontal bus and read out the digital signal, 5. Final digital signal are read out sequentially at a speed up to 280 MHz.

The camera also features two shutter modes, global and rolling shutter. These two modes can be selected trough the program interface and offer two different ways the to read the image from the sensor. In rolling shutter mode the, the charge is transferred from each row sequentially during readout. The global shuttering mode essentially reads out every pixel simultaneously resulting in the end of exposure simultaneously for all pixels. The rolling shuttering mode offers higher readout speeds and lower noise, but can lead to spatial distortion as each row will start and stop its exposure at slightly different times from its neighbour (around 10 μs). As the camera sensor is split in half and the camera reads the sensor from the middle outwards, this can lead to a difference in the readout of about 10ms at the top and bottom edges compared to the centre of the sensor. This might pose a problem if we are to take a picture of anything that is changing fast enough with time, e.g., the tissue where the amount of blood in a location might change significantly in the time taken.

2.3.2 AOTF

Different filters can be used to filter the light e.g., liquid crystal tunable filter, rotating wheel filters and acousto optical tunable filters [6, 7, 8]. The rotating wheel filter is an easy way of acquiring samples, but it needs lots of space if many wavelengths are wanted and thus is not suited for hyperspectral imaging. The optical transmitivity of the liquid crystal tunable filter is better than that of an AOTF, but the tuning speed of the AOTF is much greater than that of the liquid crystal tunable filter, and this is a huge advantage for the acquisition speed of the system [1]. The operational principle of the AOTF is based on the acoustic-optic effect, explained in Saleh and Teich [9] chapter 20 (A more detailed explanation can be found in [8]). In its essence, the acousto-optic effect states that a sound wave travelling trough a material, e.g., Tellurium dioxide(TeO_2), will compress and dilate it as the acoustic wave propagates. As the density of the material is varied along the material, its refractive index will be modulated with the acoustic wave, introducing an acousto-optic interaction between the two waves. This interaction can cause phenomena called Bragg diffraction to happen if the angle of incident is small(close or less than the Bragg condition). An image of what will happen can be seen in Figure 2.6 and the brag condition can mathematically be expressed as:

$$sin(\theta) = \frac{\lambda}{2\Lambda}, \tag{2.1}$$

where λ and Λ is the wavelength of the optical and radio wave respectively and θ is the angle of incidence. The light incident onto the crystal will have two different first order diffractions that wave orthogonal polarisation. Due to the limitations of the Bragg condition the acceptance angle of the AOTF will be small (about 2° for TeO_2 [8].

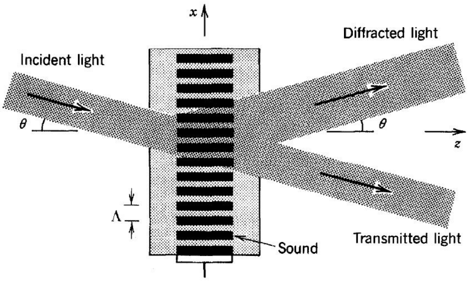

Figure 2.6: Showing the principle of Bragg diffraction.

2.3.3 Optical Path Length

The optical path length is the length, l_o, that is shortest for the light to travel trough a material of refractive index, n, and lenght, l, can be calculated as:

$$l_o = \frac{l}{n} \tag{2.2}$$

2.3.4 Aperture diameter

The aperture can be calculated from the geometry of the system and the required acceptance angle as:

$$tan(\theta) = \frac{r_D}{f} \rightarrow r_D = f \cdot tan(\theta), \tag{2.3}$$

where f is the focal length of the lens, θ is the desired angle of acceptance and r_D is the radius of the aperture.

2.3.5 Polarization

As explained in subsection 2.3.2 the output of the AOTF is polarised. Polarisation is a consequence of the vibrational state of electromagnetic radiation. Light vibrating in one plane is considered to be polarised. If the light is vibrating in more than one plane, it is considered to be nonpolarized. Polarising is the process of turning nonpolarized light into polarised light. This can be done in several ways, e.g., by reflection, refraction, scattering or transmission trough different materials. A polariser is a filter that passes light of a specific polarisation and blocks light of other polarisations. See Figure 2.7 for an image of how a wire grid polariser changes the properties of light. This change is due to the electromagnetic properties of the wires and how electrons are free to move in one direction but not the other. As a consequence, the light that passes trough a wire grid polariser has a polarisation state normal to the direction of the wires. Together with the AOTF polarisers can be used to separate the positive first order diffracted light from the non-diffracted and negative first order diffraction created in from the AOTF. To achieve this one polariser is inserted in front of the AOTF and a second is added after the AOTF in a cross-polarised configuration i.e. The first creates vertically polarised light and the second filters out all but the horizontally polarised light. A drawback of using polarises is that they will filter out much of the light and additional light might be required.

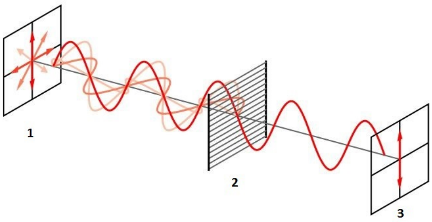

Figure 2.7: Wire grid polariser (2) converts unpolarized light from the source (1) to vertically polarised light at the output (3).

2.3.6 Pinholes

As it is important to limit the input angle of the light at the front interface of the AOTF to the acceptance angle of the AOTF (see subsection 2.3.2) and to block remaining light from the non-diffracted, light pinholes are utilised. If we place the pinholes in the front and back focal points our system will be telecentric [10] and thus give the system a magnification that is independent of the distance to the object and position in the field of view. This will also reduce radial distortion (see section 2.4).

2.4 Aberration, Noise and Calibration

Any imaging system will have some aberration and noise and thus need calibration. Some of these aberrations and sources of noise will be presented down below as well as some methods to counteract these unwanted properties.

2.4.1 Chromatic Aberrations

Chromatic aberrations can be divided into two types, namely transverse and longitudinal aberrations according to Voloshinova et al. [11]. How to reduce the effect is also proposed in the same article. Transverse aberrations are due to the diffraction angles dependence on the light wavelength and give rise to a lateral shift of the image in the plane of diffraction, with an angle γ' as depicted in Figure 2.8. Longitudinal aberrations, on the other hand, is a result of the change of optical path length in the system, due to the wavelength dependence of the refractive index in the Acousto-optical crystal in the AOTF. This form of aberration will give a shift in the plane of best image sharpness by a distance δb see Figure 2.8 and results in a defocusing of the picture. To reduce these types of aberrations, some measures can be taken. For the transversal aberrations, one can tilt the exit face of the crystal about its entrance face [11, 8] and this can only be done when the filter is produced, and a deeper mathematical explanation can be found in Voloshinova et al. [11] and Xu and Stroud [8]. The longitudinal aberrations are caused by dispersion in the AOTF and are strongly dependent on the rest of the system of which it is a part. Therefore it is suggested by [11] that the addition of a negative lens in front of the first lens (nr 2 in Figure 2.8), or a positive lens after the polariser (nr 5 in Figure 2.8), would reduce the longitudinal chromatic aberration.

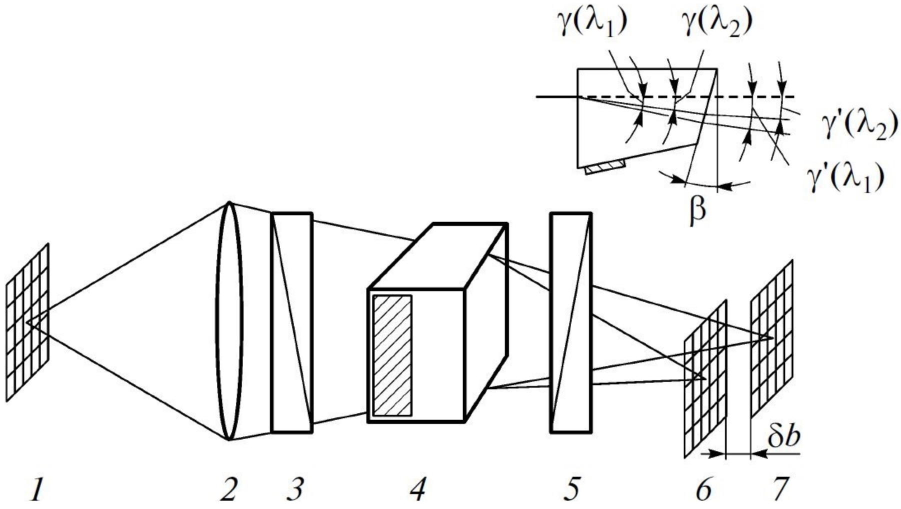

Figure 2.8: Shows the optical scheme of an system with an AOTF. 1, an object with broadband spectrum; 2, lens; 3, polariser; 4, AOTF; 5, crossed polariser; 6, image of the first diffraction order at λ_1; 7, image of second diffraction order at $\lambda_2 (\lambda_1 < \lambda_2)$. The insert shows a ray diagram of the AOTF where β is the tilt of the exit face of the crystal.

2.4.2 Radial distortion

The other main type of distortion that should be considered is the radial distortion. This type of distortion will be highly symmetrical if the system is symmetrical around the optical axis and is due to non-uniform magnification as we travel further away from the optical axis. This type of distortion is normally classified as either pincushion or barrel distortion. It is characterised as barrel distortion if the image magnification is decreasing with the distance from the optical axis the effect on a grid can be seen from Figure 2.9. In the case of pincushion, the magnification is increasing further away from the optical axis (see Figure 2.9). A third type that in reality is a combination of pincushion and barrel distortion is called moustache distortion. All three of these aberrations are quadratic with distance from the optical axis and can be corrected for using Brown-Conrady's distortion model [12] and applying software processing as long as the low order components dominate.

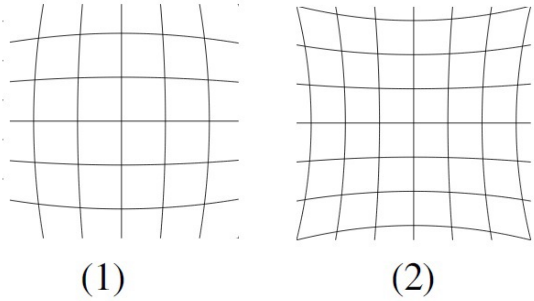

Figure 2.9: Showing barrel distortion (1) and pincushion (2).

2.4.3 Pixel nonlinearities

Since we are to use a camera sensor, noise will be generated. There will be three main sources of noise from the sensor, namely read noise, dark noise and photon noise. The read noise originates from the electronic readout process and is lower in an sCMOS sensor technology compared to normal CCD (typically 1.1 electrons for sCMOS@288MHz and 6-10 electrons for a conventional CCD@20MHz). Also, the dark noise originates from the dark current that is dependent on the temperature of the imaging sensor. The effect of the dark current can not be directly subtracted from the image to correct for it, but one can take the mean of a dark noise image and subtract this from the images. Since the dark current is thermally dependent, a way of reducing it and therefore the dark noise is to keep the sensor cool. For relatively low intensities the photon noise will be greater than the read noise, and for an even lower signal, the read noise will be more dominant than the photon noise. The read and photon noise are the two statistically dependent noise sources and can be reduced by taking multiple images and or filtering. Pixels can be divided into five different categories; Namely noisy pixels (NP), unphysical noisy pixels (UNP), hot pixel (HP), dead pixel (DP), and un-linear pixels (UP) [13]. Here NP are characterised by its higher than average noise, UNP have a noise level that has noise lower than the photon noise, HP have high dark signal, and the DP is always zero, and the UP gives a nonlinear response. Note that pixels can be in multiple groups e.g. dead pixels are also nonlinear the same is true for hot pixels. A visualisation of this can be found in Figure 2.10. To find these pixels, an integrating sphere with a broadband DC halogen lamp can be used in addition to three measurement series:

- A dark current measurement for the highest and lowest integration time used to find the DP, HP, UNP and NP types of pixels.

- One measurement at intermediate integration time used to find HP, UNP and NP types pixels.
- Some measurements at different integration times (about four should suffice) to find UP.

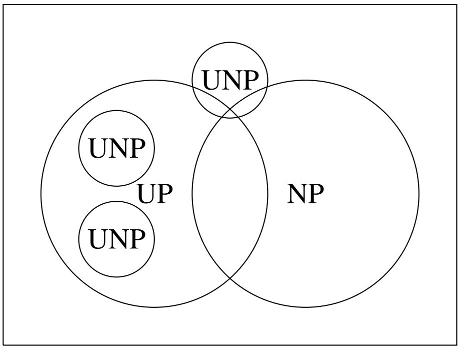

Figure 2.10: Venn diagram of the relation between pixel types

2.4.4 Noise and aberration calibration

The primary calibration of a hyperspectral camera consists of three main steps [13] to turn the raw sensor data, a digital number (DN), into absolute spectral radiance data. These are spectral calibration, bad pixel characterization and calibration, and a radiometric calibration. For spectral calibration, one would like to expose the entire field of view to a precise monochromator and scan this over the entire spectral range of the camera. This is a thorough job and requiring lots of time or an automated set-up. In practice, it is sufficient to use some discrete wavelengths and interpolate the values for the others. To get a uniform illumination of the entire field of view, an integrating sphere can be employed. And instead of the monochromator, a light source with narrow bandwidth and known wavelengths can be used (e.g. laser or gas excitation lamps). Then we can interpolate for the different wavelengths to make a calibration file. In system utilising an AOTF, the RF-intensities for each band has to be calibrated to avoid smearing in the spectral dimension. This can be done by letting the camera look into a calibrated integrating sphere and find the ratio of the average intensity in the image and divide it by the known intensity from the sphere.

$$C_\lambda = \frac{\overline{I_{image,\lambda}}}{I_{sphere,\lambda}} \tag{2.4}$$

The conversion from raw data (DN) to radiance can be done by the following equation:

$$L(i,j) = \frac{(DN(i,j) - BG(i,j)) \cdot h \cdot c}{QE(i) \cdot RE(i,j) \cdot SF \cdot t \cdot A \cdot \Omega \cdot \Delta\lambda(i) \cdot \lambda(i)} \tag{2.5}$$

Here i is the spectral band number and j spatial pixel number of the sensor, BG is the background signal (dark signal), h is the Plank constant, c is the speed of light, QE is the quantum efficiency of the whole system, RE is the relative response of each pixel, SF is a scaling factor, t is the exposure time, A is the Aperture , Ω is the solid angle, $\Delta\lambda$ represents the spectral sampling of the camera, and λ is the wavelength [13].

2.4.5 Image Registration

As the object imaged from a system that scan in the spectral range can move significantly between two acquisitions, the need for image registration rises. Image registration aligns the pixels of the individual images so that the spectral data is from the same spatial location. This can be challenging and is also dependent on the method used to capture the spectral and spatial data. Despite this variation, the majority of registration methods consists of four main steps. These are feature detection, feature matching, transform model estimation and image resampling. In the feature detection, distinct features such as edges, contours, line intersections, etc. are detected either manually or automatically and can be represented in different ways for future processing. Then a step of feature matching is performed to get a relationship between a reference image and the image to be registered. From this it is estimated a transform to get a mapping function that will align the reference to the image to be registered, this step is called transform model estimation. As the last step, an image re-sampling and transformation step are needed where the image is mapped onto the reference by using the mapping function found in the previous step [14].

2.4.6 Characteristic Parameters

A good measure of the imaging systems ability to acquire an image is the signal to noise ratio, SNR. This can be defined as the mean signal divided by the mean noise as a function of frequency.

$$SNR_\lambda = \frac{\overline{Signal}}{\overline{Noise}} \tag{2.6}$$

Where the noise will consist of the photon noise, dark noise and read noise. If the signal to noise ratio is calculated near saturation, it is called peak SNR.

Another parameter that is often used to characterise a camera or an image is the dynamic range, DR, this can be expressed as:

$$DR = 20 \cdot log_{10} \left(\frac{Level_{max}}{noise_{dark}} \right), \tag{2.7}$$

and tells us the cameras ability to reproduce the bright and dark portion of the image and how many variations it is capable of reproducing in between the two.

2.5 Light Transport in Tissue

In this section, we will have a look at skin properties and how skin can be modelled for reflectance measurements. Light propagation in tissue can be modelled in a number of ways; one is to simulate the propagation of single photons in a Monte-Carlo (MC) simulation. Another more analytic way is to use the Radiative Transport Equation (RTE) or even the diffusion approximation of the RTE [15].

2.5.1 Skin physiology

The skin is one of the largest organs of the human body and protects the body from environmental stress such as infections, dehydration, an excessive amount of optical radiation and thermal stress. The skin consists of three main layers (see Figure 2.11); epidermis, dermis and subcutis (hypodermis), all of these can be subdivided into smaller layers [16]. Instead of looking at all of the epidermal layers separately, the layers have been combined to form one layer, and the optical properties of the individual layers have been combined. The epidermis consists mainly of dead cells, and therefore there is no blood in this layer. But because the dermis-epidermis interface is not completely flat, some blood needs to be added to simulate a flat and uniform epidermal layer. This layer is approximately 100 microns thick and almost entirely independent of the location. The dermis is considered to be vascularized and contains most of the blood. This layer is from 1 to 4 mm depending on body site and age [17]. Under the dermal layer is a layer of subcutaneous fat (1-6 mm thick depending on location). Because of the limitation of the penetration depth of the light (see subsection 2.5.8), we will consider the dermal layer to be semi-infinite. For shorter wavelengths, this will not hold, and a three layer model must be used.

2.5.2 Tissue types

The distribution, size and clustering of the melanin in the skin are the main reason for the difference in skin colour on humans. This trait is genetically determined, but the colouration can change slightly with the exposure to UV radiation. Human skin can be divided into six categories according to how the skin reacts to UV exposure called the Fitzpatrick scale. The physical principle behind this colouration

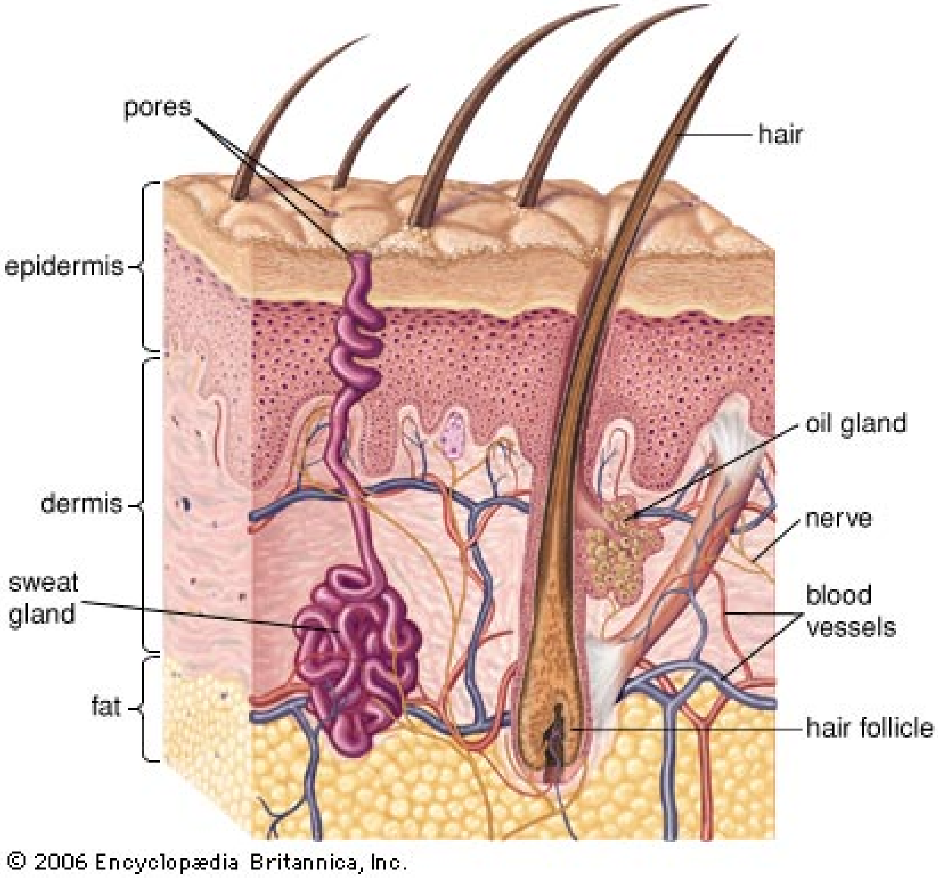

Figure 2.11: Cross section of human skin [18].

is the melanins high absorption. There is also a slight variation in scattering across skin types, but this is considered to be small enough to be left out [19].

2.5.3 Tissue location

The tissue can vary in thickness depending on body location. It can be as thin as 0.05 mm on the eyelids and behind the ear (postauricular region) to 1.5 mm thick in the palms of hands and the foot sole [20]. The difference in thickness is mainly due to different dermal thickness as the epidermal thickness is almost constant throughout life, and from one location to another [20].

2.5.4 Child Tissue

The skin of a child can be quite different from the skin of an adult. First of all, it is generally thinner than adult skin and gets progressively thicker with age [20]. The absorption is also generally lower. This is mainly because the melanin production in skin develop as the child grows, but also because the scattering properties change with age. The difference in the spectra for a Caucasian boy and girl at different ages can be seen in Figure 2.12.

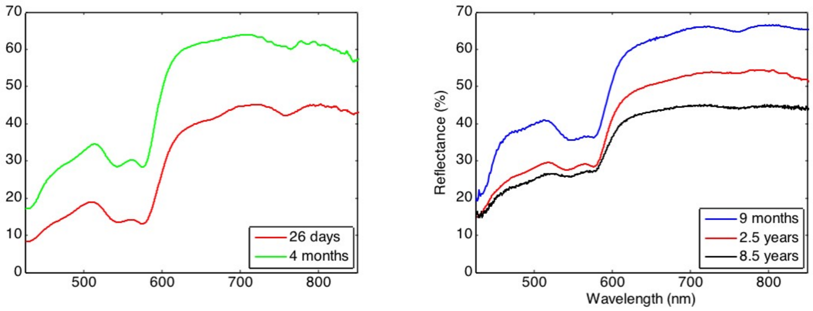

(a) **(b)**

Figure 2.12: Showing the measured skin reflectance of a Caucasian boy (a) and caucasian girl (b) at different age [21].

2.5.5 Atopic Echema

Atopic eczema also called atopic dermatitis and is a result of the interaction between genetic and environmental factors. It causes an inflammatory reaction to the skin and is characterised by dry skin (xerosis), itching (pruritus) and erythematous lesion [22]. The Erythematous lesion would cause an increase in the blood flow and therefore the oxygenation level in the affected area whereas the xerosis would cause the scattering to increase.

2.5.6 Absorption in tissue

Optical absorption in tissue is mainly due to blood (oxygenated and deoxygenated haemoglobin), melanin, fat and water. For deoxy and oxygenated haemoglobin we can see that they have distinct absorption spectra but share some points, called isobestic points. Using these points, it is possible to calculate the concentration of oxy- and deoxyhaemoglobin as well as the oxygenation level and the blood volume fraction. We can define an absorption coefficient μ_a as the probability of a photon getting absorbed in a medium per unit path length. This will result in a drop in intensity according to Beer Law

$$I(x) = I_0 exp(-\mu_a x), \tag{2.8}$$

where I is the intensity and I_0 is the intensity at $x = 0$ This leads to the definition of transmittance:

$$T(x) = \frac{I(x)}{I_0} = exp(\mu_a x) \tag{2.9}$$

This can be seen as the photons probability of surviving propagation over a distance x without being absorbed. The reciprocal of the absorption coefficient is called the mean absorption length. According to [24] the melanin absorption can be modelled approximately as

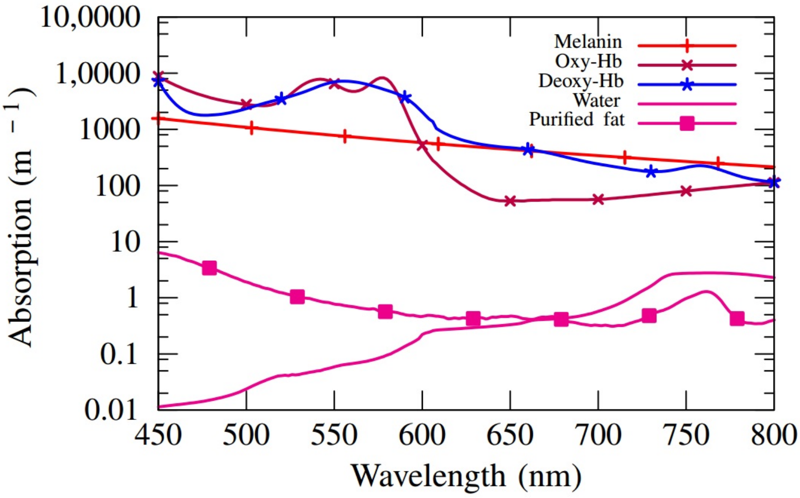

Figure 2.13: Common absorbers in tissue plotted against wavelength [23].

$$\mu_{a,m} = \mu_{a,m,normal} (\frac{694nm}{\lambda})^{3.46} \tag{2.10}$$

with $\mu_{a,m,normal} = 225m^{-1}$ for a newborn child with North European skin type

The concentration of oxygenated and deoxygenated haemoglobin can be found from:

$$\begin{aligned} \mu_a(\lambda_1) = ln(10)\epsilon_{ox}(\lambda_1)C_{ox} + ln(10)\epsilon_{de}(\lambda_1)C_{de} \\ \mu_a(\lambda_2) = ln(10)\epsilon_{ox}(\lambda_2)C_{ox} + ln(10)\epsilon_{de}(\lambda_1)C_{de} \end{aligned} \tag{2.11}$$

At two different wavelengths λ_1 and λ_2 this can be used to calculated the oxygenation saturation given by:

$$S_{O_2} = \frac{C_{ox}}{C_{ox} + C_{de}} \tag{2.12}$$

and the total concentration of haemoglobin, also referred to as the blood volume fraction

$$C_{Hb} = C_{ox} + C_{de} \tag{2.13}$$

2.5.7 Scattering in tissue

The biological scattering originates from photon interaction with structures such as cell membranes, cell nuclei and mitochondria. Here cell nuclei and mitochondria are the primary scatterers in tissue. The scattering is most prominent when the structures are of the same size as the optical wavelength and have a refractive index mismatch. Scattering occurs when photons interact with a spherical particle of any size and can be modelled exactly by the Mie theory. For particles that are much smaller than the wavelength in question, Mie theory is simplified to Rayleigh theory. If the scatterers are sparsely distributed, that is where the mean distance between particles are much greater than the wavelength and the size of the scatterers, and the medium is considered to be loosely packed. Otherwise, the medium is considered densely packed. In the case of densely packed mediums, the scattering event is coupled, and single scattering theory does not apply. In the case of loosely packed mediums, the single scattering theory applies and each scattering event is considered independent of each other. From this, we can define a scattering coefficient μ_s as the probability of photon scattering in a medium per unit path length. The scattering mean free path is then defined as the reciprocal of μ_s. We can also define the transmittance for the scattering, similar to that of absorption, as:

$$T(x) = exp(-\mu_s x) \tag{2.14}$$

This is also called the ballistic transmittance because it describes the probability of a photon propagating a distance x without scattering.

According to [25] the reduced scattering coeffecient have been measured to follow these equations:

$$\mu_s' = \mu_s'(mie) + \mu_s'(rayleigh) \tag{2.15}$$

where

$$\begin{aligned} \mu_s'(Mie) &= A\{[1 - (1.745 \cdot 10^{-3}\lambda)] + (9.843x10^{-7})\lambda^2\} \\ \mu_s'(Rayleigh) &= B\lambda^{-4} \end{aligned} \tag{2.16}$$

From tabulated values in [25] A and B are found to be 70 and $9.25 \cdot 10^{11}$ respectively, for skin of a newborn and both would be greater for older children.

For different skin types, the scattering coefficient only changes slightly. In the shorter wavelength regions (600-800nm) the scattering is the main contribution to the reflectance spectrum in this region as shown by Zonios et al. [26]

It is also useful to know, when we are looking at multiple scattering events, the angular distribution of the scattering events and the distance between them. This distance, between scattering events, is called the scattering mean free path l_s and is given by the reciprocal of the scattering coefficient $l_s = 1/\mu_s$. It is dependent on the amount of scattering particles and also the distance between them. The angular distribution is given by an anisotropy factor g, defined as the average cosine of the scattering angle:

$$g = \overline{cos\theta} \tag{2.17}$$

Where θ is the scattering angle. From Gemert et al. [27] this factor is given as

$$g_e \approx g_d \approx 0.62 + 0.29 \cdot 10^-3\lambda \tag{2.18}$$

where λ is in nm and is approximately 0.8 in the optical range. The reduced scattering coefficient is given by:

$$l_s' = \frac{l_s}{1-g} \tag{2.19}$$

At this depth the photons have lost all information about their incident direction. We can then define the reduced scattering coefficient, μ_s' as:

$$\mu_s' = \frac{1}{l_s'} \tag{2.20}$$

2.5.8 Penetration Depth

The photons ability to penetrate deep into the tissue is a function of its wavelength, for longer wavelengths the photons will penetrate deeper into the tissue. This effect is seen as a result of the scattering and absorption in the tissue. The mathematical definition can be seen from Equation 2.32 in subsection 2.5.10

2.5.9 Radiative Transport Equation

Definitions

Spectral radiance is the energy flow per unit normal area, per unit solid angel, per unit time, per unit temporal frequency bandwidth, or the amount of energy given off as radiation of different frequencies. Radiance L is then defined as the spectral radiance integrated over a narrow frequency range.

$$L(\vec{r}, \hat{s}, t) = L_\nu(\vec{r}, \hat{s}, t)\delta\nu \tag{2.21}$$

Fluence rate is defined as the energy flow per unit area per unit time. It is not dependent on the flow direction and can be expressed as:

$$\Phi(\vec{r}, t) = \int_{4\pi} L(\vec{r}, \hat{s}, t)d\Omega \tag{2.22}$$

The time-integrated fluence rate is called fluence, F:

$$F(\vec{r}) = \int_{-\infty}^{+\infty} \Phi(\vec{r},t)dt \tag{2.23}$$

Current density $\vec{J}$ is defined as the net energy flow per unit area per unit time and can be expressed as:

$$\vec{J}(\vec{r},t) = \int_{4\pi} \hat{s}L(\vec{r},\hat{s},t)d\Omega \tag{2.24}$$

From these definitions and the principle of conservation of energy we can derive the Radiative Transport Equation (RTE):

$$\begin{aligned}\frac{\partial L(\vec{r},\hat{s},t)/c}{\partial t} =& -\hat{s}\cdot\nabla L(\vec{r},\hat{s},t) - \mu_t L(\vec{r},\hat{s},t)\\ &+ \mu_s\int_{4\pi} L(\vec{r},\hat{s}',t)P(\hat{s}'\cdot\hat{s})d\Omega' + S(\vec{r},\hat{s},t),\end{aligned} \tag{2.25}$$

where the term on the left-hand side is the change in energy in the volume element. The first term on the right-hand side is the divergence of energy out of the same volume element. The second term is the energy loss in the volume element, and the third term is the scattering into the volume element. The fourth term is the energy produced by a source in the volume element. All terms are per unit time.

2.5.10 Diffusion equation

From the RTE (Equation 2.25) a diffusion equation can be derived. This is an proximate solution to RTE when the scattering is much stronger than the absorption ie. $\mu_s \gg \mu_a$, also called high-albedo. This solution assumes an almost isotropic light distribution within the tissue. Then the radiance, L, can be expressed as an series expansion:

$$L = \frac{\phi}{4\pi} + \frac{3}{4\pi}\vec{j}\cdot\vec{s} + ... \tag{2.26}$$

where $\vec{j}$ is the photon flux vector and ϕ is the fluence rate. The first term on the right hand side is the series expansion of the isotropic radiance, and the second term is the deviation from isotropy in the direction given by the unit directional vector $\vec{s}$. The irradiance on the surface normal to the flux can be expressed as:

$$E = \frac{\phi}{4} \pm \frac{j}{2} \tag{2.27}$$

Where plus is for a surface facing the direction of the flux and the minus is valid for surfaces facing away from the direction of the flux. The diffuse photon flux, $\vec{j}$, is given by Fick's law:

$$\vec{j} = -\zeta \nabla \phi \tag{2.28}$$

Here ζ is the diffusion constant given as:

$$\zeta = \frac{1}{3\mu_{tr}} = \frac{1}{3(\mu_s(1-g)+\mu_a)} \tag{2.29}$$

Where μ_{tr} is the transport coefficient, μ_s, μ_a are the scattering and absorption coefficients and g is the scattering anisotropy.

Under steady state the continuity equation can be expressed as:

$$\nabla \cdot \vec{j} = -\mu_a \phi + S \tag{2.30}$$

Where S is the source density for diffuse photons. Equation 2.28 and Equation 2.30 can be combined to form te steady state diffusion equation:

$$\begin{gathered} \mu_a \Phi(\vec{r},t) - \nabla \cdot [\zeta \nabla \Phi(\vec{r},t)] = -S(\vec{r},t) \\ \nabla^2 \Phi - \frac{\Phi}{\delta^2} = \frac{S}{\zeta} \end{gathered} \tag{2.31}$$

Here δ is the effective attenuation coefficient:

$$\delta = \sqrt{\frac{1}{3\mu_{tr}\mu_a}} \tag{2.32}$$

And the reciprocal of δ is the penetration depth in diffusion theory.

For a time-independent point source it can be shown [15] that the solution to Equation 2.31 is:

$$\Phi(\vec{r}) = \frac{1}{4\pi\zeta r} \cdot exp(\delta r) \tag{2.33}$$

Boundary conditions between two scattering media can be expressed by continuity of the irradiance in the forward and backwards directions.

$$\begin{gathered} \frac{\phi_1}{4} + \frac{j_1}{2} = \frac{\phi_2}{4} + \frac{j_2}{2} \\ \frac{\phi_1}{4} + \frac{j_1}{2} = \frac{\phi_2}{4} - \frac{j_2}{2} \end{gathered} \tag{2.34}$$

At the skin-air interface a useful boundrary condition can be obtained by setting the reflected part of the irradiance at the skin-air boundary equal to the irradiation propagating back into the skin (see Haskell et al. [28] for a detailed method on how this is done):

$$R_{eff}(\frac{\phi}{4} + \frac{j}{2}) = \frac{\phi}{4} - \frac{j}{2} \tag{2.35}$$

Here R_{eff} is the effective reflective coefficient that can be found by integrating the Fresnel coefficients for non polarized light over all angles of incidents from inside the skin. For the diffusion theory to be valid the flux has to be less than the fluence rate, which is only partly true at the skin surface. The error produced by this is small enough so that we can still use the diffusion theory [28].

Chapter 3

Instrumentation System

In the below the camera system will be explained briefly, that is what the main components is used for and how the parts were acquired.

3.1 Camera System

The overall system as outlined in chapter 2, discussed in this section and seen from Figure 3.14, was mounted on a custom frame made at the Tele engineering workshop. This frame was made to be fitted on a camera stand. The assembled imaging system can be seen from Figure 3.5 and a figure of the overall system with measurements can be found in Figure 3.14.

3.1.1 Pinholes

The pinholes are included in the system to stop stray rays and limit the incoming rays to the acceptance angle for the AOTF (pinhole 1). They also function as a secondary stop for the 0-th order light that passes trough the Acousto optic tunable filter (pinhole 2). To limit the system to the acceptance angle of the AOTF Equation 2.3 was used with $\theta = 2^{\circ}$ and the placement of the pinhole at the focal point of the front lens found in [29] to be $35mm$ gives $r_D = 1.22mm$. To make the system telecentric another pinhole, with the same radii, was put after the second lens at the focal point. The pinholes were constructed at the Tele engineering workshop (Trondheim, Norway) to fit the lenses and can be seen from the Figure 3.1.

3.1.2 Polarisers

There are two wire grid polarisers in the system, both are WP25M-UB wire grid polarisers from ThorLabs (Newton, NJ, US), one right before the first lens and one on the lens following the AOTF. The first polarizer is to polarise the incoming

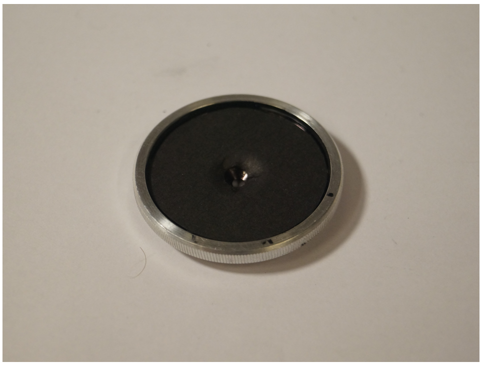

Figure 3.1: Image of the pinhole in front of lens 1.

light to be vertically polarised before entering the AOTF so that all the first order light is horizontally polarised and the 0th order is vertically polarised. The second polariser will stop the 0th order light from reaching the camera. Test done by [1] got a better extinction ratio if the polarisers were placed between the pinholes and lens in stead of between the lens and filter as suggested by [11] and the polarisers were placed accordingly.

Figure 3.2: Image of Lense, Lense coupler and polariser from left to right.

3.1.3 Lenses

The system consists of three MeVis-C 1.6/35 lenses from Qioptiq (Paris, France). They work together with the pinholes to form a telecentric confocal system. The lenses are machine vision lenses for cameras with up to 12Mpix sensors, and they are designed to limit radial and chromatic aberrations.a picture of one of the lenses can be seen in Figure 3.2. To calculate the placement of the lenses we have some limitations. First, the system is required to be confocal that is the focal point of the first and second lens should coincide inside the AOTF. This gives us the dependency on the optical path. The distance the light have to travel trough the crystal to get to the centre is given by Equation 2.2, with $l = l_{filter}/2$ and $n = n_{TeO_2,\lambda=644nm}$, where $n_{TeO_2,\lambda=644nm}$ is the refractive index of the AOTF crystal at a wavelength in the middle of the spectrum we are interested in, resulting in:

$$l_o = \frac{20.75}{2.2565} = 9.20mm \tag{3.1}$$

where $l_{filter}/2$ is from the datasheet of the lens [29] and $n = n_{TeO_2,\lambda=644nm}$ from [30]. From the datasheet of the lens, the distance from the back of the lens to the focal point can be found to be at a distance 14.7 mm from the back of the lens subtracting 9.2mm yields 5.5 mm from the crystal surface to the lens surface. This also holds for the second lens. The third lens should be placed such that its front focal plane coincides with the back focal plane of the second lens. The total distance between the lens surfaces should be 14.7 mm + 11.9 mm = 26.6 mm.

3.1.4 AOTF and Driver

The main part of the system is an AOTF and a Radio Frequency driver (RF-driver). The AOTF is a TF625-350-2-11-BR1A from Gooch & Housego (Ilminster Somerset, UK) and will split the light so that we can investigate one wavelength at a time. The Filter is constructed using a TeO_2 crystal and its refraction index can be found in a lookup table [30]. The filter has been tested and confirmed to conform with the information provided by the manufacturers [1]. A mathematical description of this particular filter can be found in Stedham et al. [31]. The RF-driver, an AODS 20200-8 part nr. 97-03926-12 also from Gooch & Housego is computer controlled through a USB interface and can be set to a selected frequency at will. Commands that can be sent to it is described in [32].

Figure 3.3: Image of the AOTF and driver.

3.1.5 Coupler

The two back lenses are held together with a machined piece of brass made by the Tele engineering workshop. This piece is also sand blasted and tinted black to cause fewer reflections in the system. In addition to being a coupler between the two lenses is it also serves as a holder for the second polariser and as the second pinhole. The inside of the coupler can be seen from Figure 3.4 and a side view is seen in Figure 3.2.

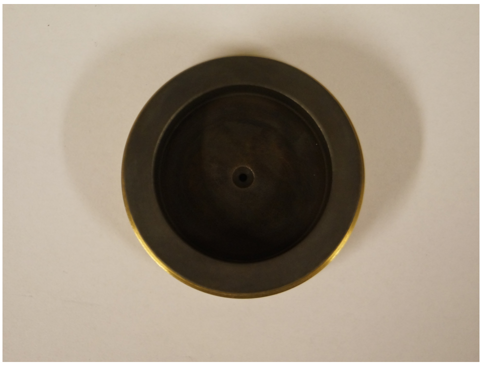

Figure 3.4: Image of the lense coupler for MeVis lenses. This part also serves as a pinhole and holder for a polarising filter.

3.1.6 Camera

The camera utilised is a Zyla 5.5 sCMOS camera from Andor Technology (Belfast, UK), it features an sCMOS sensor that is thermoelectrically cooled to ensure low readout noise due to dark currents. It also has a large dynamic range and, rapid frame rate, hight quantum efficiency and a large field of view. Tests have been performed by Castrillo [1] to compare this camera to a CMOS camera (EMCCD iXion Ultra) and also to the manufacturer's specifications, and it was found to be compliant. The camera is operated through a Camera Link interface to the same computer that controls the RF-driver for the AOTF. There is also a driver library for the camera that can be found online [33] The camera can be seen to the left in Figure 3.5.

3.1.7 Lamp

A portable studio lamp, Lykos Bicolour from Manfrotto (Cassola, Italy), was used to illuminate the subjects. The spectrum from this lamp can be seen from Figure 3.7(b) and when set to 50/50 this creates a relatively flat spectrum see Figure 3.7(b). The lamp was rated at 1500 lux at 1 meter.

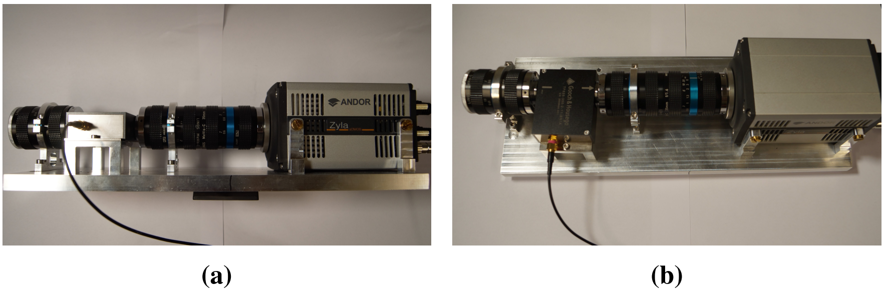

(a) (b)

Figure 3.5: Image of the Andor Zylas camera system used. Viewed from (a) the side and (b) from an aerial view.

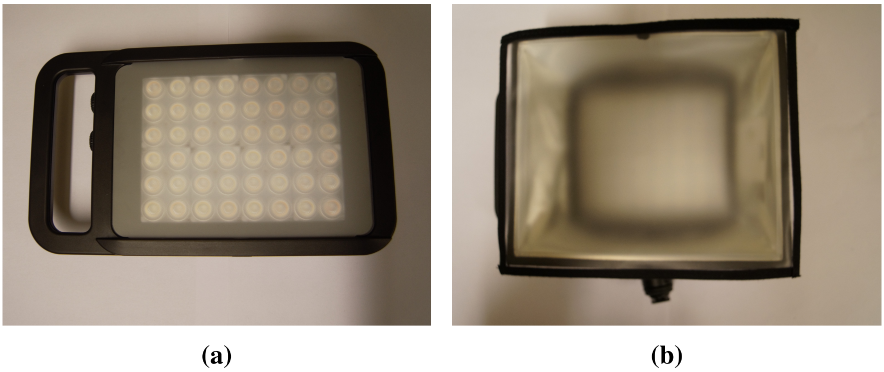

(a) (b)

Figure 3.6: Showing (a) the lamp with only one diffusor and (b) the lamp with both diffusors.

3.2 Test Targets

Test targets were bought to assess the systems resolution, spectral response, chromatic aberration, radial distortion and depth of field. There are altogether four targets, a USAF1951 resolution target, a Macbeth colour checker target, a dot target and a depth of field target. The USAF1951 test target is for measuring resolution, to use this target one would take a picture of the target and read out the resolution from where the lines on the target start to blend. The target can be seen from Figure 3.8(a). The Macbeth target, seen from Figure 3.8(b), gives a known spectral response for each of the squares. The spectra from each square can be compared to the known spectra of the target. A dot target is used to check the radial distortion, where the alignment of dots in the physical target will be compared to the alignment of the imaged target. This difference can then be used to calibrate for this distortion, and Figure 3.8(c) shows this target. Lastly, the depth of field target, Figure 3.8(d), is used to assess the depth of field of the system. This is done by

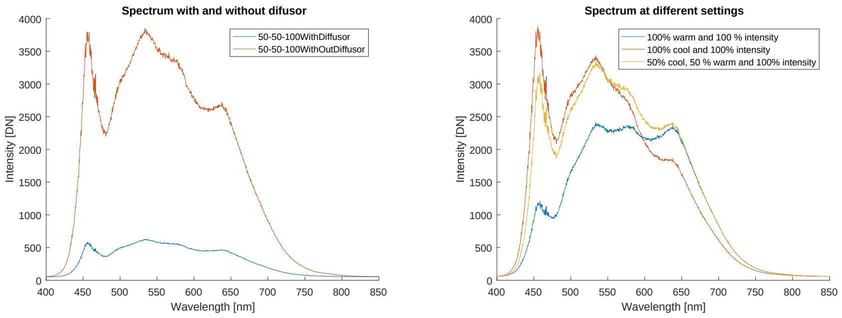

(a) **(b)**

Figure 3.7: Showing the relative intensity in the lamp spectra with and without a diffusor (a) and the relativ intensity spectrum of the lamp at different settings (b).

taking a picture of the target and then read of the depth of field directly.

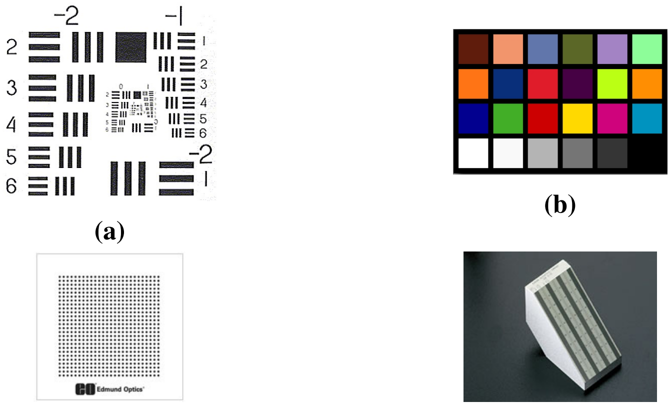

(a) **(b)**

(c) **(d)**

Figure 3.8: Test targets:(a) USAF1951 resolution test target, (b) Machbeth ColourChecker test target for testing spectral response, (c) Dot target for measuring aberration, (d) Target for measuring depth of field. Images from [34, 35, 36, 37].

3.3 Spectrometer

A USB4000 spectrometer from Ocean Optics (Duiven, Nederland) together with an Ocean Optics ISP-ref integrating sphere was used to acquire the spectrometric data from the children. Before each measurement series the spectrometer and integrating sphere, the spectrometer was calibrated using a 99% white standard(SRT-99-050) from labsphere (NH, US). The spectrometer was also used with a fiberoptic probe to acquire the spectrum of the lamp. Besides a USB2000 spectrometer from Ocean Optics was used for measuring the lamp- and colour target spectra.

(a) (b)

Figure 3.9: Image of (a) the Ocean Optics Spectrometer and (b) integrating sphere used.

3.4 Software

The main bulk of the code used is based upon the work of others, a crude user interface has been developed by [1], and the fitting code has been developed trough multiple projects in biomedical optics at the Norwegian University of Science and Technology [23, 38]. A link to a git repository containing the code can be provided upon request.

3.4.1 Image Possessing

After the images had been acquired, image processing was done to improve the quality, alignment and to remove noise. The processing steps can be seen from Figure 3.10 where there is some human interaction. First, a raw data image was taken as an input. Then the background (dark image) is subtracted for all bands before the image is filtered using an averaging filter to reduce noise. After this, a region is chosen by the user, and a mean is calculated for each band. Then the white standard image is multiplied by the spectral response of the white standard; this result is stored for later use on multiple images acquired in a small time interval. Almost the same procedure is done with the raw image of the object. First, the background is subtracted then an averaging filter is applied before the image is divided by the reflectance standard image already calculated. The last step is to normalise the values before image registration is done and the spectra are extracted.

3.4.2 Image Registration

The images have been registered by use of a registration software developed by Viste [39]. Images before and after image registration can be seen from Figure 3.11 and Figure 3.12. A grid has been overlayed to make the shift more visible.

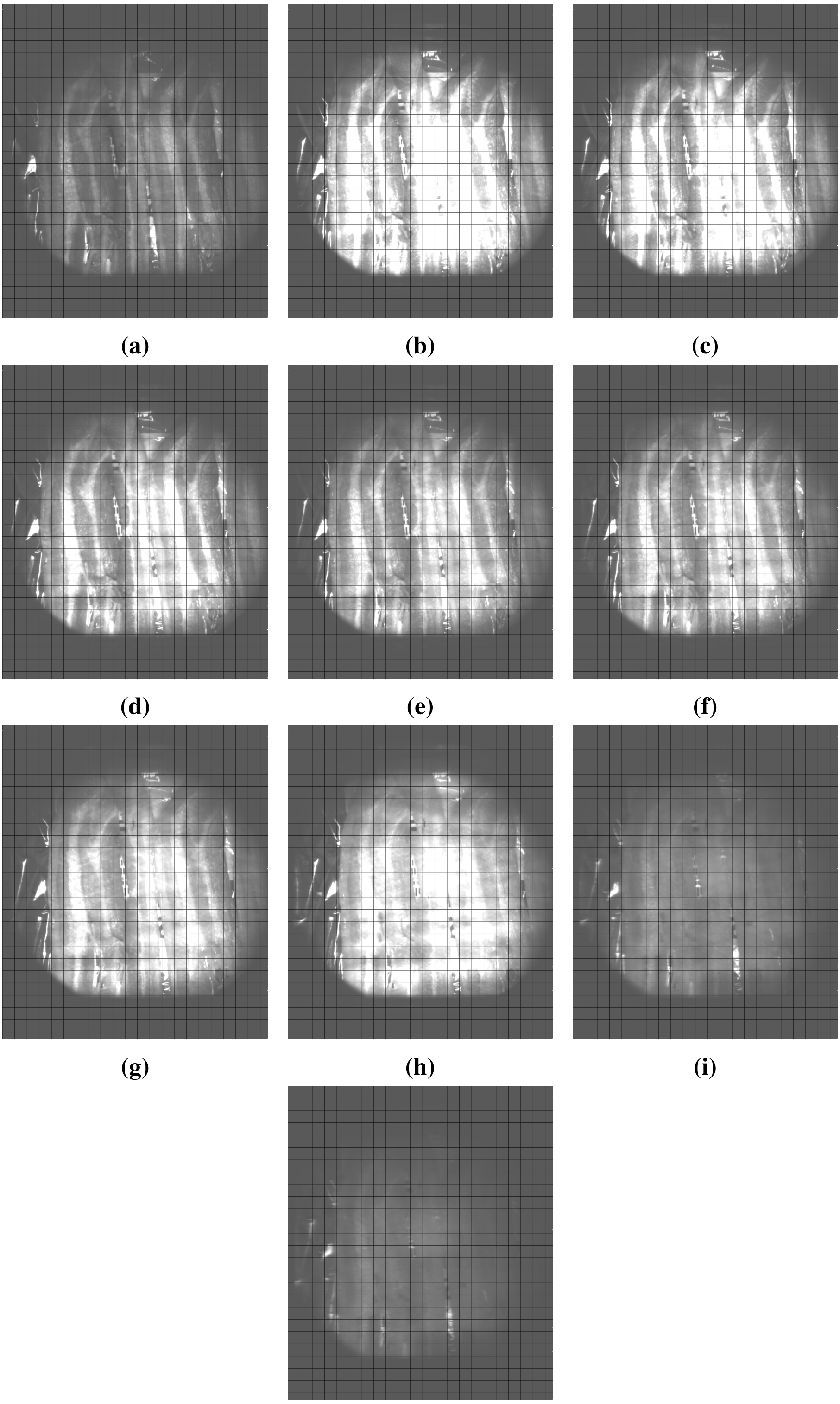

(a) (b) (c)

(d) (e) (f)

(g) (h) (i)

(j)

Figure 3.11: Images of bacon before image registration

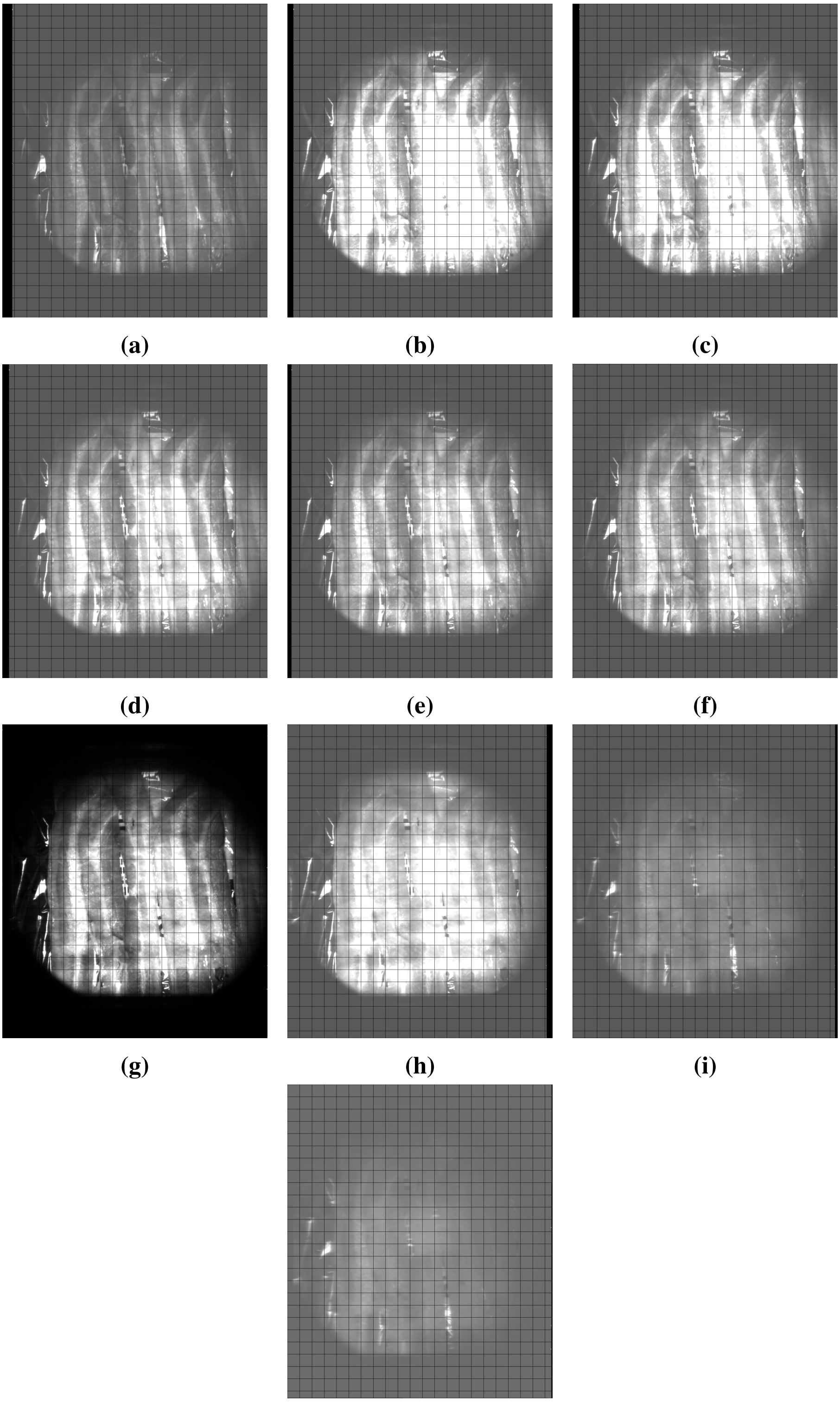
(a) (b) (c) (d) (e) (f) (g) (h) (i) (j)

Figure 3.12: Images of the same bacon as in Figure 3.11 but here the images has been registered and normalized a second time.

3.4.3 Spectra fitting

After the image has been registered and the reflectance found, the spectral information can be extracted. The same method as described in Bjorgan et al. [23] are used, and the basic outline of the steps can be seen in Figure 3.13. We first find the spectra of normal skin and is done using the two-layer diffusion model with initial parameters. This spectrum was manually compared, and adjusted, to the normal skin samples from the patients trying to get the initial parameters set correctly. A spectrum of the skin with eczema was used as input and fitted using a linear last square method with non-negative constraints to get the concentration of the absorbers. From this the blood volume fraction and oxygenation can be calculated according to Equation 2.12 and Equation 2.13.

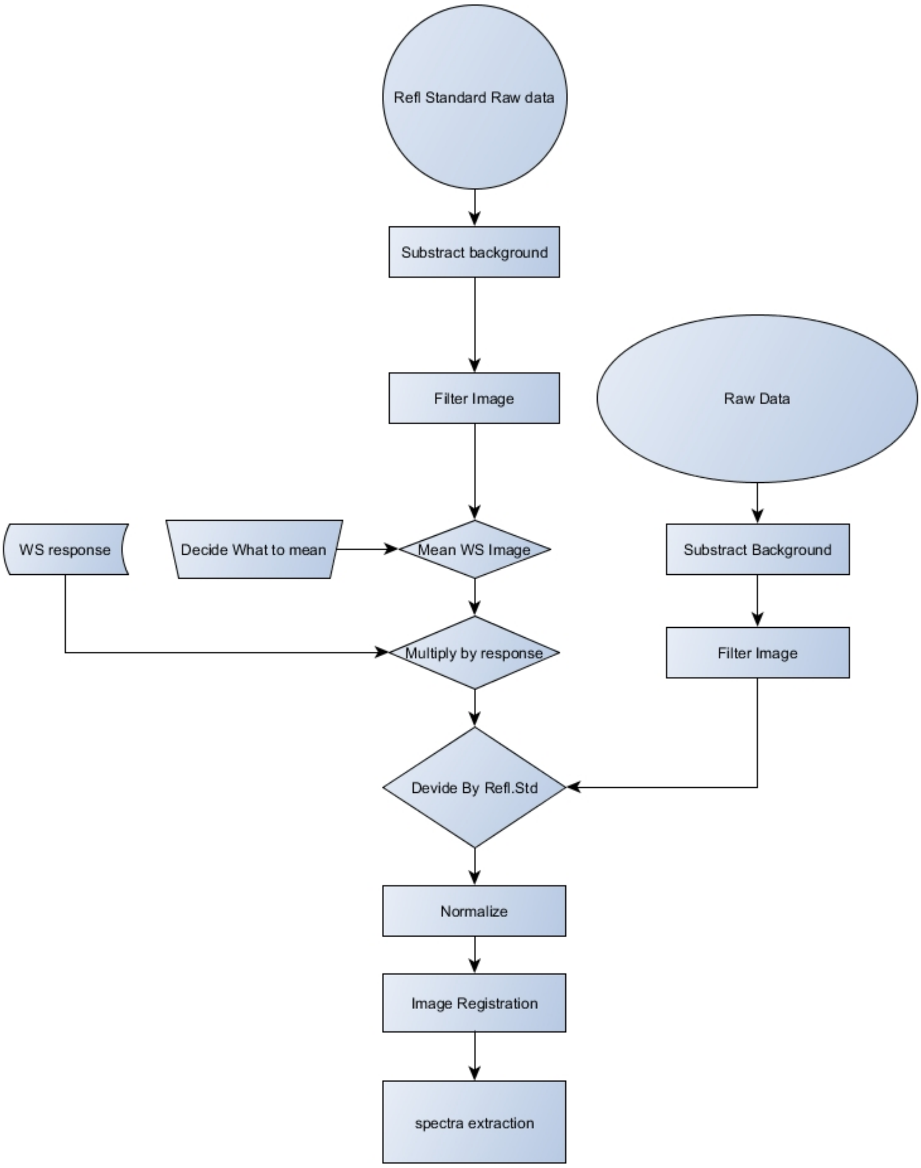

Figure 3.10: Flow chart of the image processing

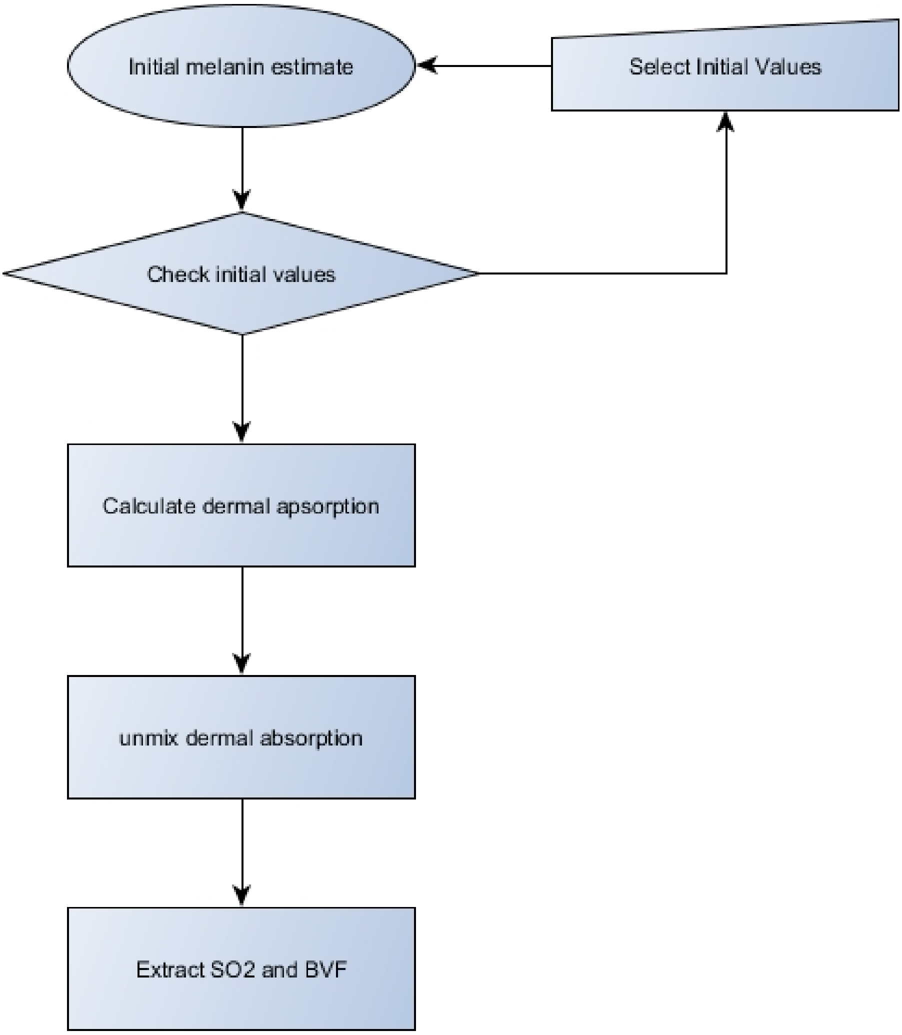

Figure 3.13: Spectral Processing

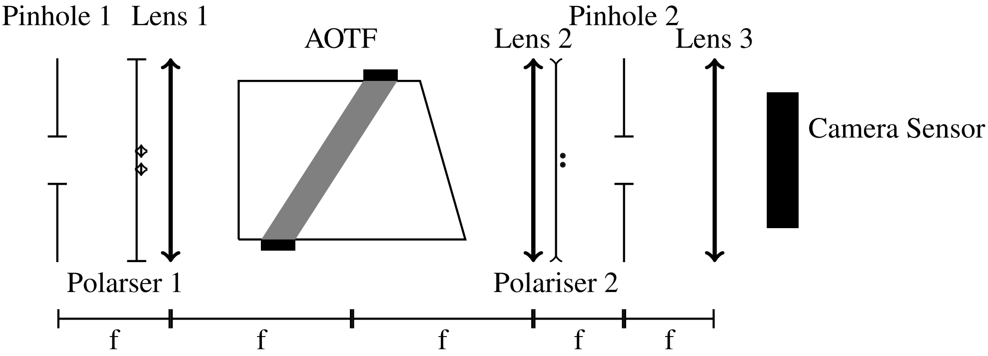

Figure 3.14: Optical System. Here f is the focal length of the three lenses used.

Chapter 4

Data Acquisition protocol

In this section, a description of how the images and spectra were acquired will be presented so that the reader can repeat the measurements with ease.

Spectra from children have been gathered twice and images once. The quality of the pictures was so bad that they could not be used, see chapter 5. Therefore some images of bacon were acquired to assess the capabilities of the camera. Here a protocol for how the images and spectra were captured will be presented. All measurements of spectra were acquired by use of the same spectrometer as described in section 3.3 and measurements from the camera has been acquired using the constructed imaging system described in section 3.1. Before the data acquisition trips to measure on patients was made, ethical approval was given by the "Regional committee for medical and health research ethics - South East" [40].

4.1 Oslo

Two trips were made to gather data, both to Oslo. On the first trip, measurements were done using a spectrometer only, on the second trip acquisition with the camera and spectrometer was done.

On both occasions, the set-up was put together and tested before the children arrived. At arrival, the children were let to play, while a doctor would assess the eczema, and the measurement set-up and procedures were explained to the parents. This was done to acclimatise the patients to the temperature and new environment so that the measurements would be accurate and the children would be less scared and afraid. The acclimatisation was shorter for the first trip to Oslo, and this was noticeable on the children as they were much quieter and calmer the second time. Pictures of the children's affected area would be taken as the children were on their parent's lap to help calm the children and thus reduce movement. The camera was set to acquire eight images with an exposure of 0.1 seconds per wavelength, with the lamp on 50/50 on the spectra setting and 100% intensity and amplitude of the RF-driver was set to 50%. Also, it was found that the lighting in the room had the same spectral response as the Lycos lamp so this was left on as extra illumination. After the images were acquired, the spectrometer would be used to obtain spectra at the same body location with and without eczema. The number of images and spectra acquired was dependent on the child mood, activity level, and how severe the eczema was. If the child was calm and relaxed some additional spectra were obtained from the back, thigh, stomach or cheek as a reference for future work. In between measurements, the light source in the integrating sphere was turned off to let it cool down, the surface of the integrating sphere was disinfected, and the spectrometer was calibrated. At the start and end of the day, an image of a white standard was acquired with the camera. Throughout the measurement period, images was acquired at; 480 nm, 542 nm, 548 nm, 555 nm, 576 nm, 585 nm, 600 nm, 660 nm, 760 nm, 800 nm and 805 nm.

Figure 4.1: The imaging setup used in Oslo on the second trip. Slightly out of focus, in the front, the lamp can be seen. In focus is the camera (with a rubber duck on top), and in the background, the RF-driver and spectrometer can be seen. The main computer is set on the table to the left in the background.

4.2 Arm

To compare the camera with other systems an arm was imaged before, during and after the blood to the arm had been occluded with a sphygmomanometer. Three images were acquired, and this time the camera was set to an exposure time at 10 seconds with the RF-driver at 100%, the light spectrum set at 50/50 and the intensity of the lamp to 100%. Besides a spectrometer was used to check the oxygenation in the arm and used as a reference. One image of the arm was acquired as a baseline; then the sphygmomanometer was inflated until the artery was completely occluded. The spectrometer was checked regularly, and when the spectrum stabilised another image was acquired. After 4 minutes the sphygmomanometer was deflated, and a third image was taken. All images were acquired at the following wavelengths; 480 nm, 542 nm, 548 nm, 555 nm, 576 nm, 585 nm, 600 nm, 660 nm, 760 nm, 800 nm and 805 nm.

4.3 Misc Lab

Multiple images have been acquired at the laboratory. These images have been acquired using different settings, and exactly what they were will be described when the data are presented in chapter 5. There have been some similarities as both the imaging system and the illumination has been kept the same for all experiments.

Chapter 5

Results and Discussion

In the following section, results will be presented and discusses. It has been acquired data on children two times, first with only spectrometer and then with a camera and spectrometer. The children had various skin types, and this will be seen clearly in the spectra and the RGB-images.

5.1 Images

5.1.1 DOF Target

There have been difficulties in getting a sharp focus of the imaging system. This is thought to be a consequence of the placement of the lenses in front and the back of the AOTF . This, together with lots of internal reflections, leads us to believe that the entire optical system has to be redesign and the MeVis lenses to be exchanged with other lenses designed specifically for this system.

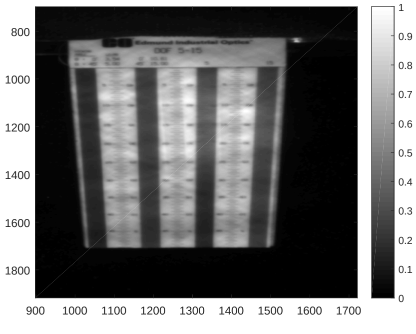

Figure 5.1: Showing an aquired image of the DOF target.

5.1.2 USAF1951 Target

A picture of the USAF1951 test target was acquired at a wavelength in the centre of our range (640 nm) to assess the resolution of our system. The entire image can be seen from Figure 5.2(a) and a cropped version in Figure 5.2(b). To find the resolution we need to find the group and element where the lines are not resolvable any more. As we can see from the images, this can be difficult, but it has been decided from visual inspection of the image that group 1 element 1 is the resolvable limit and from tabulated values supplied with the target this equals to a resolution of 2.0 lp/mm. This procedure should ultimately be done for each band to check the resolution at different optical frequencies as this can vary.

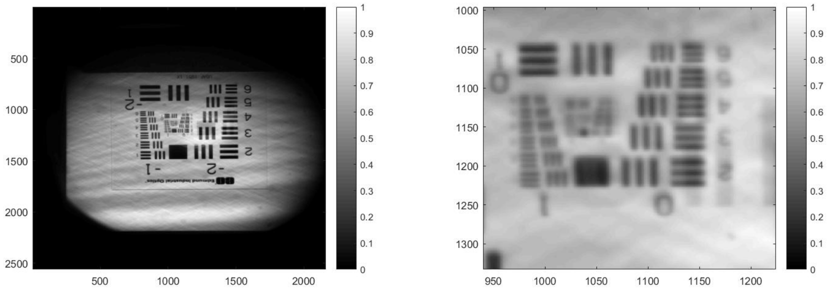

(a) **(b)**

Figure 5.2: Showing (a) the full image of the USAF1951 test target, and (b) the cropped version of the same image.

5.1.3 Colour Target

An image of the colour target was acquired and the mean of the colour regions was calculated for each band. Then the band was plotted against a spectrum measured with a spectrometer. The different regions where the mean was acquired can be seen form Figure 5.3(b). The comparison of the images vs spectrometer spectra can be seen from Figure 5.4. As we can see there are a few similarities and trends in the spectra but there are also significant differences. This is presumably caused by bad and not thorough enough calibration as well as misalignment in the system causing internal reflection.

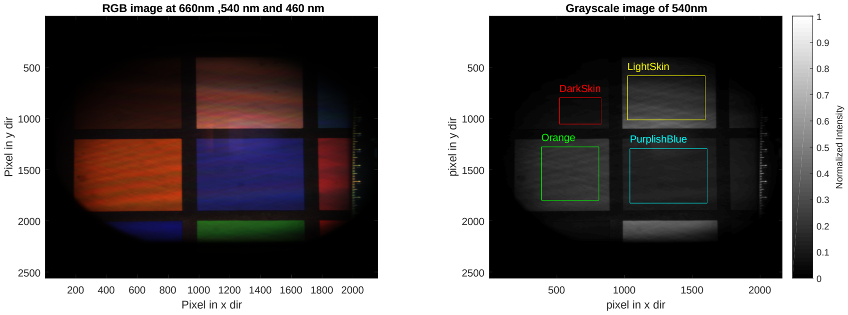

(a) **(b)**

Figure 5.3: Showing grayscale and colour image of the colour target

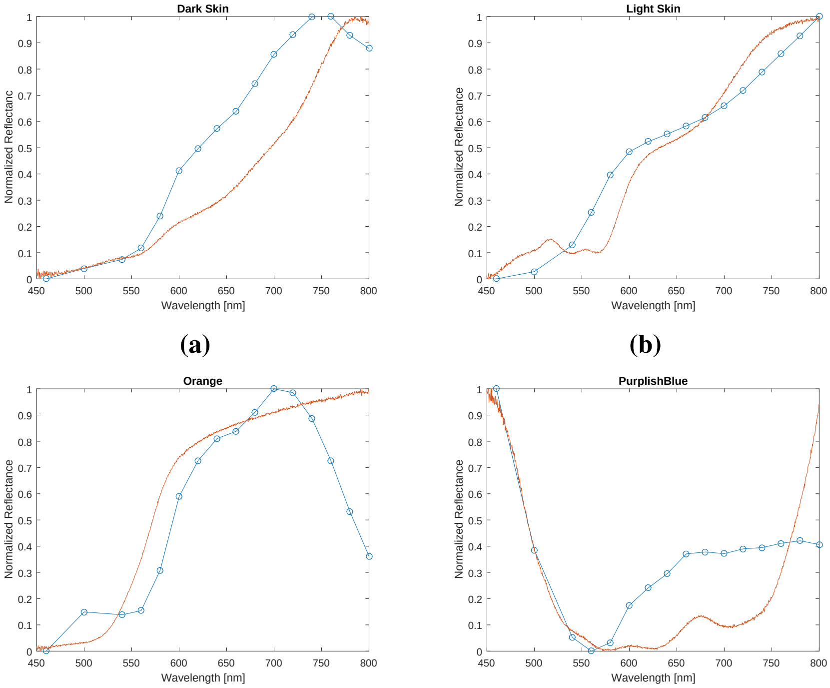

(a) **(b)**

(c) **(d)**

Figure 5.4: Spectra acquired by a spectrometer (orange) and spectra from imaging system (blue) both normalized to be between zero and one for comparison

5.1.4 Dot Target

A dot target was acquired for assessment of the distortion in the images. Due to problems with the camera system and internal reflections this calibration procedure was not fully developed, although some image processing was done to extract the dots from the image as seen in Figure 5.5. The radial calibration procedure still needs work.

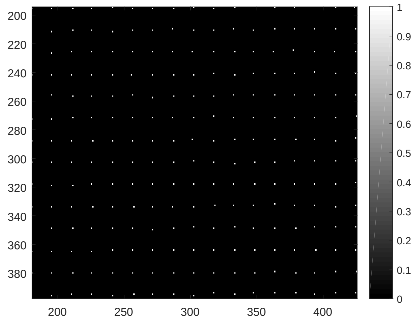

Figure 5.5: Showing the processed image of the dot target in a small part of the image.

5.1.5 Child Images

These images were acquired using an exposure time of 0.1 second and full illumination from the Lycos lamp. From the pictures, we can see that there are lots of noise, but we can also see that there is some information in them as we can see the body parts in them. The signal to noise ratio is low in all images, and also the dynamic range is low, something that is thought to be a consequence of the short exposure time and too little illumination. There is a possibility that spectral information can be extracted from such an image, but this will require the application of extensive calibration and characterization of the imaging system as well as advanced prepossessing techniques. An example of a set of images acquired in Oslo can be seen from Figure 5.6. The image has been normalised but not registered, and the dynamic range has been calculated to be 0.66 dB, this is right above the noise floor.

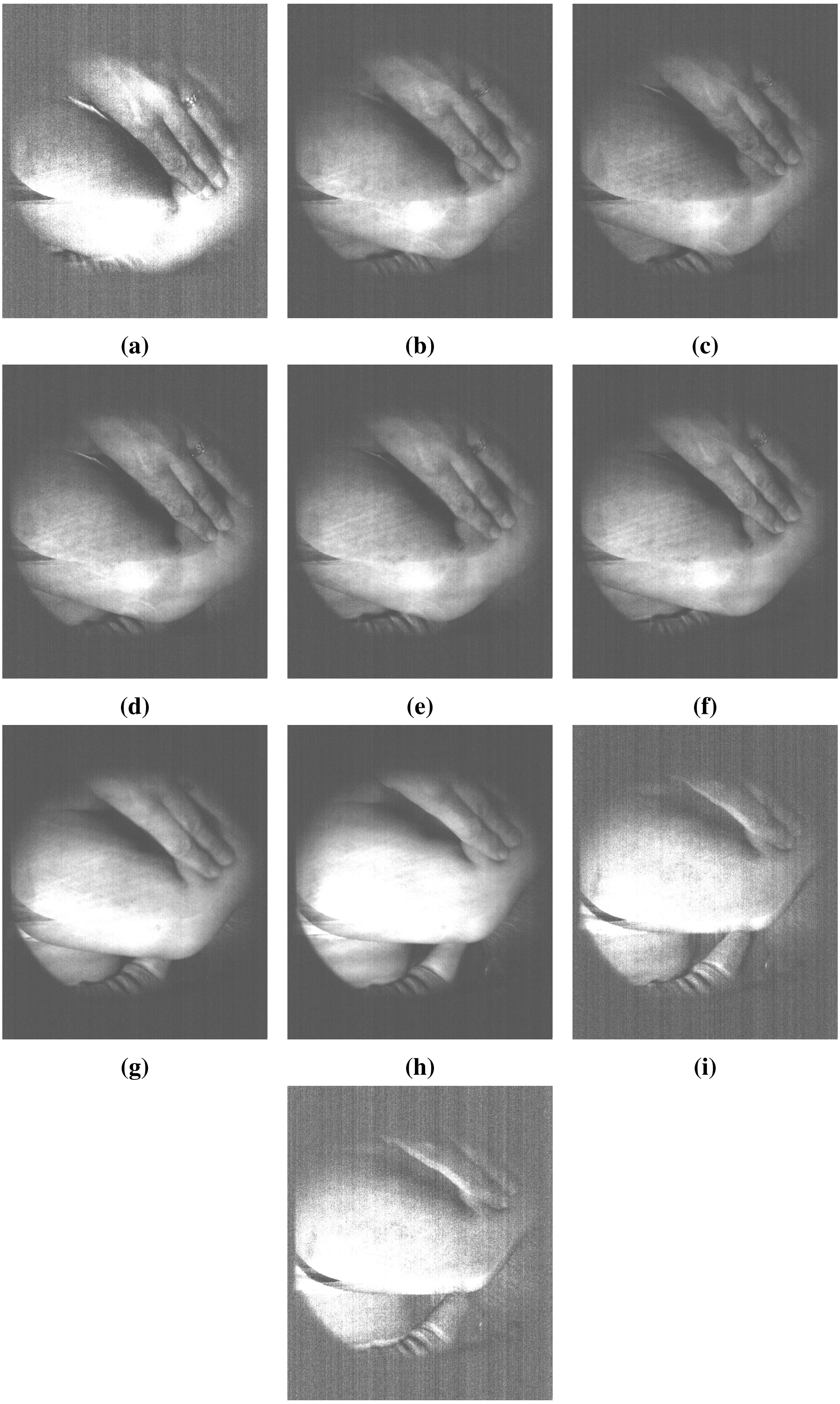

(a) (b) (c) (d) (e) (f) (g) (h) (i) (j)

Figure 5.6: Image of patient 2's thigh. The images are normalized but not registered and the dynamic rang has been calculated to 0.66 dB, just above the noise floor.

5.2 Spectra

Overall from the spectra gathered there is a tendency for eczema to give a greater change in the lower bound (500-600 nm) and to be approximately equal in the higher regions (600-800 nm) as we can see from fig.5.8-fig.5.17. This suggests that the eczema is occurring near the surface of the skin. We can also see that the difference between maxima and minima in the spectra in the 550-580 nm range is greater on the skin with eczema, which points to a higher oxygen saturation in the area. Also in the lower range, the spectra are generally lower in the area with eczema compared to the areas without. This is taken as a sign that there is more blood in the tissue in the affected area for this range. In the upper range, on the other hand, the spectra of eczema and healthy skin are similar to each other or even mixed. This suggests that the deeper layers of the tissue are not affected by eczema to the same extent. This is as expected from what we know about the how the eczema are affecting the skin and is also similar to psoriasis (see fig 3 in Randeberg et al. [41]).

It is also worth mentioning that the model used is depending on a high albedo and that the model is on edge of this region. Thus making the model less correct for skin that are very dark as in patient 3.

5.2.1 Arm

In Figure 5.7 six different spectra from the occlusion test are presented. These spectra are acquired from a female adult. As we can see the baseline spectra looks normal with descent oxygenation (two dips in the spectra around 550 nm) and a sharp increase around 600 nm as the skin of this person is rather fair. On the onset of occlusion, we can see that the spectra start to fall slightly more below 600nm than above. This can be attributed to the fact that we are occluding the vein leading the blood out of the arm, which results in more blood in tissue and an increased absorption, therefore reduced reflectance. It is also worth mentioning that the oxygenation in the outer layers (epidermis) loses oxygen fastest as there is little blood her. As time passes the oxygen in the trapped blood is used, and we can see this by the flattening of the maxima and two minima around 550 nm the three are transformed into one minima. Now the deoxyhaemoglobin is dominant in the blood; we can also see that the entire spectra drops as the oxygen is used and more blood is gathered in the tissue, and the oxygen deeper down in the tissue is used. When the occlusion is lifted, we can see a rapid return to normal conditions as expected when the fresh oxygenated blood rushes in again. It should also be noted that the spectra use a long time to get back to normal and this can also be seen from the back to normal spectra where the curve is lower in the lower spectral ranges and overshoots in the long wavelength region.

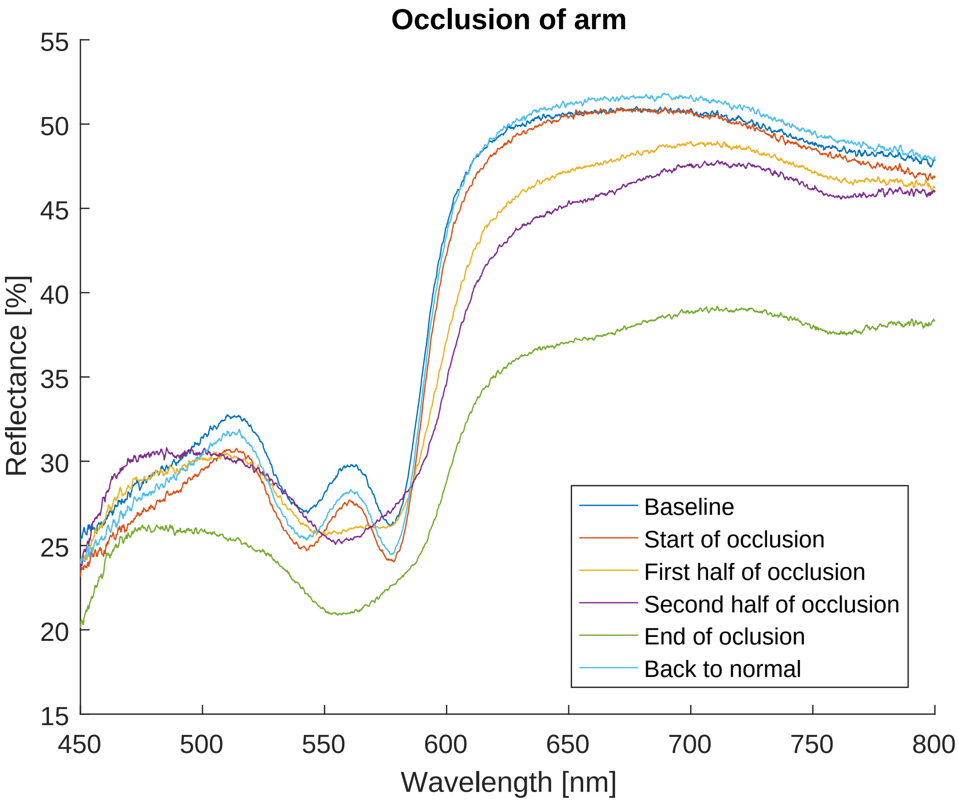

Figure 5.7: Showing the temporal response of an arm where the veins have been occluded.

5.2.2 Patient 1

Patient 1 was a girl two years of age with fair skin. Only the spectra for the patient's thigh is plotted as the other spectra would be different due to the different locations. We can see from Figure 5.8 that the spectra of normal tissue are lower than that of tissue with eczema in the entire spectral range. This is typical if there are more blood in the area, as seen in Figure 5.7. But this change is not equal for the entire range. At lower wavelengths, the difference is greater, something that is typical for more superficial erythema. Another sign of the eczema being mainly superficial is the greater amount of oxyhaemoglobin in the lower region of the spectra (two minimas at the absorption peak of oxyhaemoglobin at 542 and 577 nm). In this case, we can also see that the oxygenation in the deeper tissue (longer wavelength) is lower than for the eczema as the eczema spectra have a more evident drop in reflectance around 760 nm. This is one of the absorption peaks of deoxyhaemoglobin, leading us to believe that this eczema also affects the deeper layers of the tissue. Some spectra from other parts of the patient's body were also acquired and are compared to different body location and with other patients spectra in Figure 5.18.

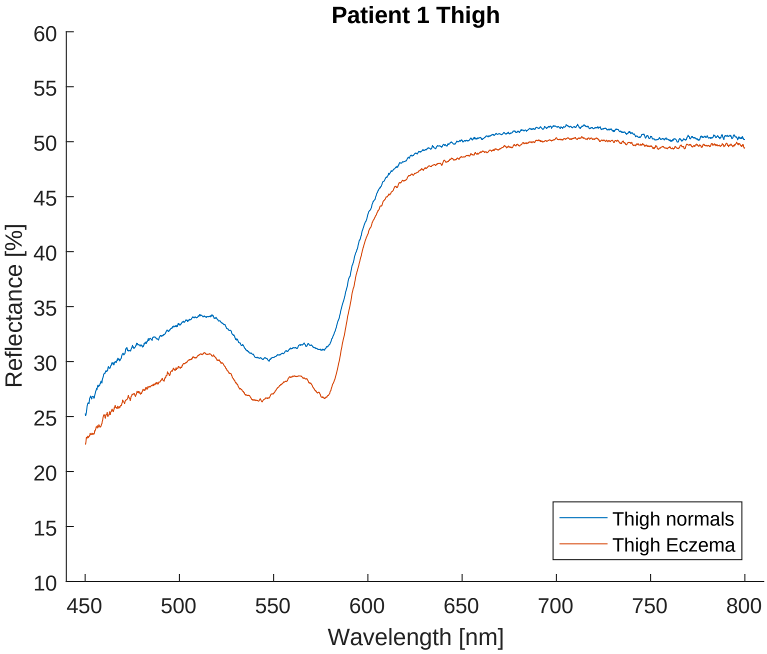

Figure 5.8: Spectra acquired for first patient.

(a) **(b)**

Figure 5.9: Images of the sampled area of patient 1. (a) is from the back and (b) is of the thigh.

5.2.3 Patient 2

Patient 2 was a girl one years and two weeks old with fair skin (see Figure 5.11). We can see the same trends in these spectra (Figure 5.10) as in those for patient 1, but the eczema is not as severe resulting in only a change in the shorter wavelength region (450-600 nm). With the greater change of the overall reflectance in the 450-600 nm region, the skin is irritated in the superficial regions.

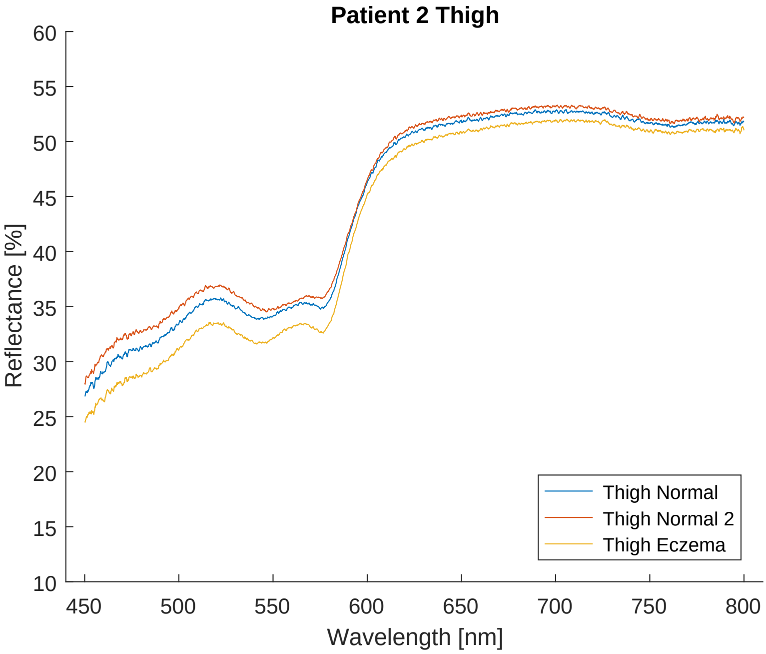

Figure 5.10: Spectra acquired for second patient.

Figure 5.11: Image showing the sampled area of the thigh of patient 2.

5.2.4 Patient 3

Patient 3 was a boy four months- and three weeks old with dark skin. This patient had reacted to an applied salve and had been hospitalised. From the spectra in Figure 5.12 we can see that the curve have a significantly different form than that of the other patients, this is because of the added absorption of the melanin giving this child his darker skin. It should be noticed that the relative difference in the spectra in the high and low region suggests that in this patient the irritation is deeper. The oxygenation higher in the skin can also be seen from this patient, but there is only a slight difference. It can also be noted that the eczema spectrum is lower, probably as a result of more blood in the area.

A spectrum of the normal tissue at the back of this patient was also acquired and is compared with other location in Figure 5.18 as an eczema spectrum was not obtained.

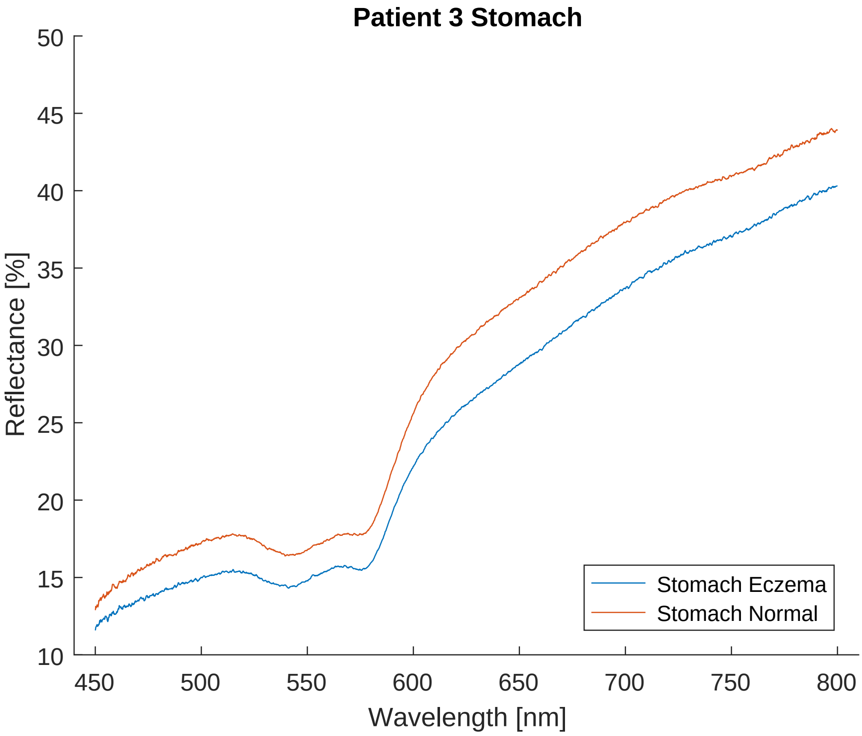

Figure 5.12: Spectra acquired for the stomach of patient 3.

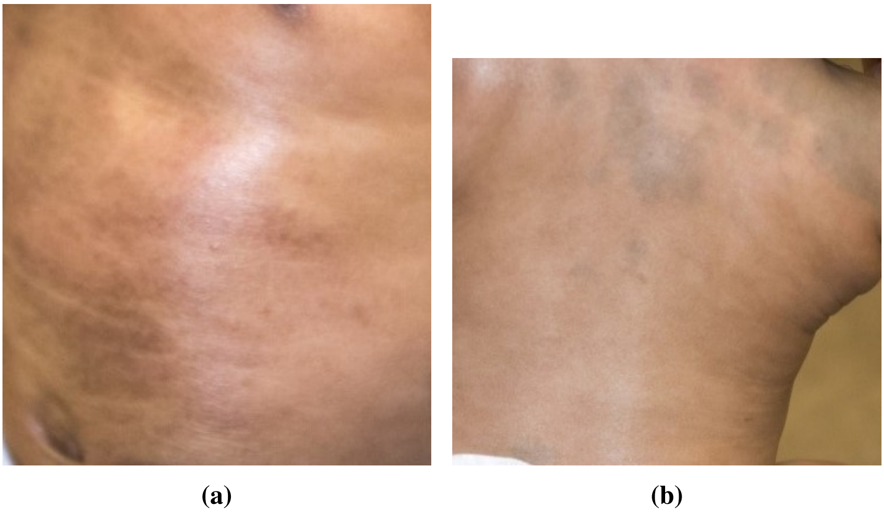

Figure 5.13: Images showing the sampled area of patient 3. (a) shows the stomach of the patient and (b) shows the back of the patient.

5.2.5 Patient 4

Patient 4 was a girl nine months and two weeks old with very fair skin. The patient did not have any visible eczema at the point of acquisition. Therefore, a spectrum of the patients back was acquired as a reference for very pale skin. This can be seen as the steep inclination around 600 nm in addition to the high reflectance in the lower region (450-600 nm). This spectrum is rather low for a patient with such fair skin, although this can be a consequence of the tissues development with age, see Figure 2.12. No more spectra of this child were acquired because the child was not found of the measurements and would not sit still. This can also be an explanation for why the spectra are so low, as we would expect a higher reflectance for wavelengths above 600 nm. It is assumed the integrating sphere was not held tight enough to the skin so that the red light would "leak" out of the sphere. Another sign of this leakage is that the noise in the upper region is greater than in the spectra acquired from the other patients.

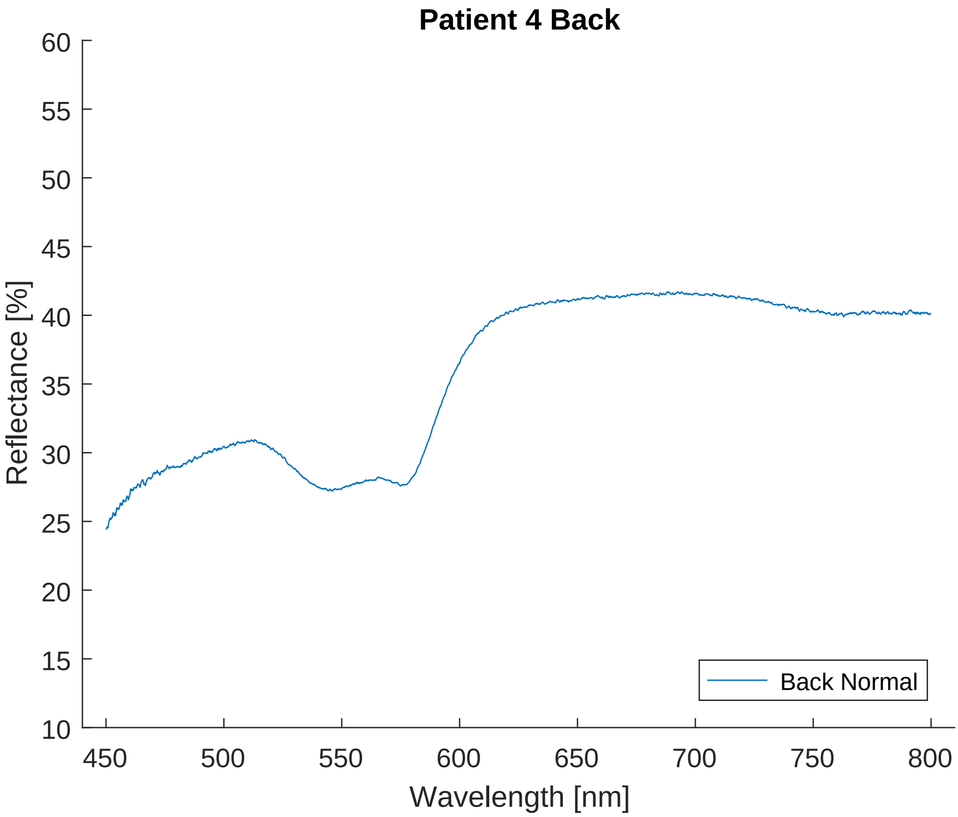

Figure 5.14: Image showing the sampled spectra of patient 4.

Figure 5.15: Image of the back of patient 4.

5.2.6 Patient 5

This patient is from the first measurement trip to Oslo where three spectrometer samples were acquired from each location, from skin with and without eczema. This patient was a boy seven months of age. From the back of the patient, we can see that one of the normal samples overlaps with one of the normal samples in addition to the rest of the measurements to have quite big spread. This is an example of how difficult it is to place the integrating sphere in the correct location and get a good measurement.

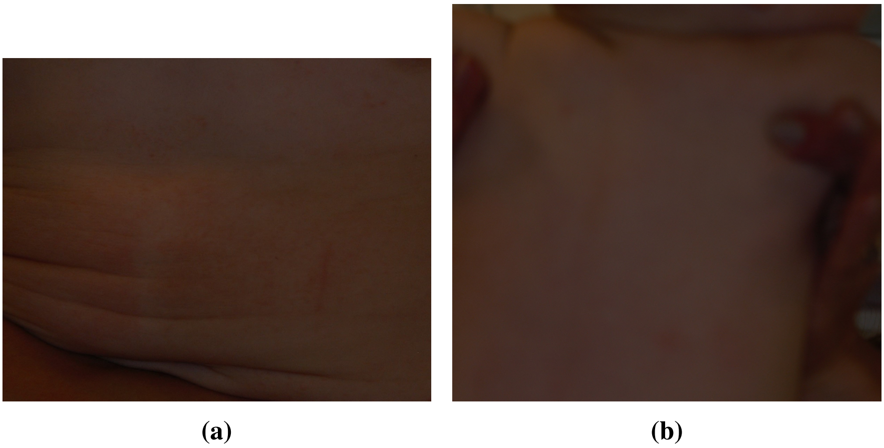
(a) (b)

Figure 5.16: Images showing the sampled area of patient 5. (a) the stomach of patient and (b) the back of the patient. (Slightly out of focus. But the eczema are still visible in the lower right and upper left of the patients back).

If a camera system had been used, we would expect similar spectra on the border between eczema and the normal tissue. But for the same tendency as for the other patients there is greater oxygenation closer to the surface of the tissue, and also more blood as the dimples around 550 nm and the overall eczema spectrum is lower than that of the healthy skin. This can be seen extremely well from Figure 5.17(b).

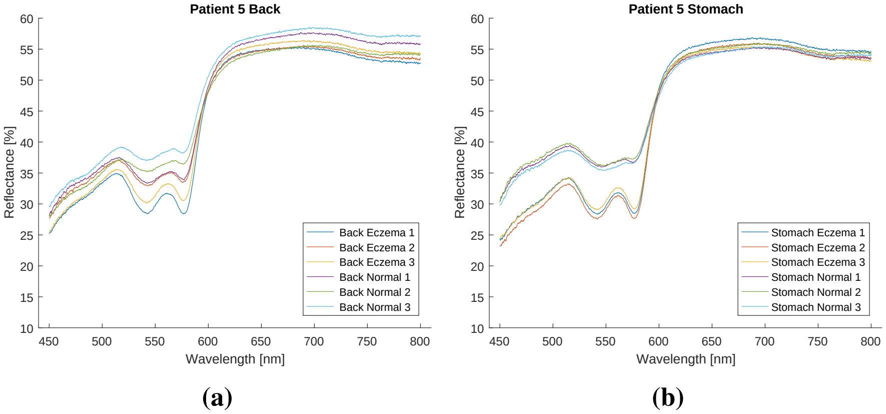

Figure 5.17: Spectra of normal skin at (a) the patients back and (b) the patients stomach.

Comparison

We have gathered some of the spectra at different location, with and without eczema, to compare the similarities and difference between patients and location. From Figure 5.18(a) we see that the difference in oxygenation in the vicinity of 550 nm in the eczema spectra for patient 1 and 2 is reasonably big. This in addition to the overall lower spectra for patient 2 in the same area (less blood in shallow skin layers), suggests that the eczema is more severe in patient 1 than in patient 2 which is also the case if we look at the pictures Figure 5.9(b) and 5.11.

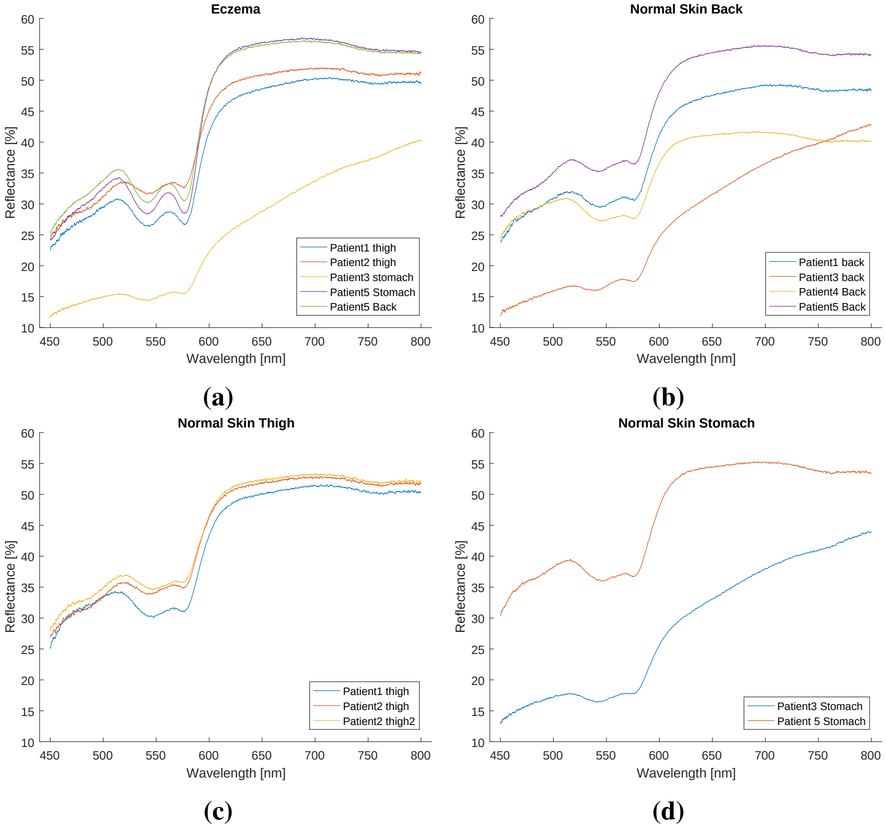

(a) (b)

(c) (d)

Figure 5.18: Showing the (a) spectra of tissue with eczema, (b) normal tissue at the back of the patients, (c) normal tissue at the thigh of the patients and (d) shows the normal tissue at the patients stomach.

Chapter 6

Conclusion and Future Work

6.1 Conclusion

It is concluded that atopic dermatitis can be detected and, with high probability, the severity assessed by use of spectroscopic methods. Although this will require more data to be statistically significant. The main characteristics of atopic dermatitis is a higher oxygenation level and more blood in the upper parts of the tissue. Also, it can be seen deeper as an increased amount of blood and deoxygenation in the tissue. There is still a need to quantify these findings, and more data has to be gathered to achieve this. To assess a large area fast and with accuracy, there are still work to be done, as the proposed and constructed camera system will not do, and therefore has to be redesigned, although the theory would allow for such a system to be constructed.

6.2 Future Work

In the following list, proposals for tasks of future work has been compiled in no particular order.

- Acquisition of more patient data to do statistical analysis on the spectra.
- Construction of a new lens system where physical dimensions of filter, polarisers, lenses, fittings and camera are accounted for.
- Incorporate calculation of erythema index, calculation of melanin index in addition to the oxygenation and blood volume fraction.
- Development of a fitting model for absorbers in tissue based on statistical analysis.

- Limit internal reflections in the camera system by using non-smooth surfaces in the internal optics as well as anti-reflective coatings where possible.
- Redesign of a user interface, that is highly modular and can be easily modified and customised.

Bibliography

[1] A.B. Castrillo. *A Hyperspectral Imaging System using an Acousto-Optic Tunable Filter*. Master thesis, NTNU, 2015.

[2] Charles Kittel. *Introduction to Solid State Physics*. Wiley, 2004.

[3] Qingli Li, Xiaofu He, Yiting Wang, Hongying Liu, Dongrong Xu, and Fangmin Guo. Review of spectral imaging technology in biomedical engineering: achievements and challenges. *Journal of Biomedical Optics*, 18(10):100901–100901, 2013. doi: 10.1117/1.JBO.18.10.100901. URL `http://dx.doi.org/10.1117/1.JBO.18.10.100901`.

[4] *BIL, BIP, and BSQ raster files*, 2017. `http://desktop.arcgis.com/en/arcmap/10.3/manage-data/raster-and-images/bil-bip-and-bsq-raster-files.htm` [Accessed:2017-01-20].

[5] Gregory P Asner, Robert S Haxo, and David E Knapp. *Computing for analysis and modeling of hyperspectral imagery*. Chapman and Hall Press: New York, NY, USA, 2008.

[6] Nahum Gat. Imaging spectroscopy using tunable filters: A review. *Proceedings of SPIE*, 4056, 2000.

[7] M.A. Afromowitz, J.B Callis, D.M Heimbach, L.A. DeSoto, and M.K. Norton. Multispectral imaging of burn wounds: A new clinical instrument for evaluating burn depth. *Transactions on Biomedical Engineering*, 35(10), 1988.

[8] Jieping Xu and Robert Stroud. *Acousto-Optic Devices*. Wiley-Interscience, 1992.

[9] B.E.A Saleh and M.C Teich. *fundamentals of photonics*. John Wiley I& Sons, 2007.

[10] D.R. Suhre, L.J. Denes, and N. Gupta. Telecentric confocal optics for aberration correction of acousto-optic tunable filters. *Applied Optics*, 43(6):6, 2004. doi: 10.1364/AO.43.001255.

[11] V. Voloshinova, K. Yushkovb, and T. Yukhnevicha. Compensation for chromatic aberrations in acousto-optic systems used in spectral analysis of images. *Moscow University Physics Bulletin*, 67(05):437–442, 2012. ISSN ISSN 0027-1349. doi: 10.3103/S0027134912050141.

[12] Duane C. Brown. Decentering distortion of lenses. *Photogrammetric Engineering*, 32(3):444–462, 1966.

[13] I. Baarstad and T. Løke. Calibration and characterization of hyperspectral cameras, 2014.

[14] Barbara Zitová and Jan Flusser. Image registration methods: a survey. *Image and Vision Computing*, 21(11):977 – 1000, 2003. ISSN 0262-8856. doi: http://dx.doi.org/10.1016/S0262-8856(03)00137-9. URL `http://www.sciencedirect.com/science/article/pii/S0262885603001379`.

[15] Lihong V Wang and Hsin-i Wu. *Biomedical optics: principles and imaging*. John Wiley & Sons, 2012.

[16] Standley W. Jacob, Clarice A. Francone, and Walter J. Lossow. *Anatomi og fysologi*. Universitets Forlaget AS, second edition, 1985. ISBN 80-00-28640-1. URL `http://urn.nb.no/URN:NBN:no-nb_digibok_2007062801003`.

[17] A N Bashkatov, E A Genina, V I Kochubey, and V V Tuchin. Optical properties of human skin, subcutaneous and mucous tissues in the wavelength range from 400 to 2000 nm. *Journal of Physics D: Applied Physics*, 38(15):2543, 2005. URL `http://stacks.iop.org/0022-3727/38/i=15/a=004`.

[18] Human skin, 2015. `https://global.britannica.com/science/human-skin` [Accessed:2017-01-32].

[19] Simon Alaluf, Derek Atkins, Karen Barrett, Margaret Blount, Nik Carter, and Alan Heath. Ethnic variation in melanin content and composition in photoexposed and photoprotected human skin. *Pigment Cell Research*, 15 (2):112–118, 2002.

[20] Skin anatomy, 2015. `http://emedicine.medscape.com/article/1294744-overview`[Accessed:2017-01-23].

[21] Lise Lyngsnes Randeberg, Bjørn Skallerud, Neil E.I. Langlois, Olav Anton Haugen, and Lars Othar Svaasand. *The Optics of Bruising*, pages 825–858. Springer Netherlands, Dordrecht, 2011. ISBN 978-90-481-8831-4. doi: 10.1007/978-90-481-8831-4_22. URL `http://dx.doi.org/10.1007/978-90-481-8831-4_22`.

[22] Michael J. Cork, Simon G. Danby, Yiannis Vasilopoulos, Jonathan Hadgraft, Majella E. Lane, Manar Moustafa, Richard H. Guy, Alice L. MacGowan, Rachid Tazi-Ahnini, and Simon J. Ward. Epidermal barrier dysfunction in atopic dermatitis. *Journal of Investigative Dermatology*, 129 (8):1892 – 1908, 2009. ISSN 0022-202X. doi: http://dx.doi.org/10.1038/jid.2009.133. URL `http://www.sciencedirect.com/science/article/pii/S0022202X15344420`.

[23] Asgeir Bjorgan, Matija Milanic, and Lise Lyngsnes Randeberg. Estimation of skin optical parameters for real-time hyperspectral imaging applications. *Journal of Biomedical Optics*, 19(6):066003, 2014. doi: 10.1117/1.JBO.19.6.066003. URL `http://dx.doi.org/10.1117/1.JBO.19.6.066003`.

[24] Thorsten Spott, Lars O Svaasand, RE Anderson, and PF Schmedling. Application of optical diffusion theory to transcutaneous bilirubinometry. In *BiOS Europe'97*, pages 234–245. International Society for Optics and Photonics, 1998.

[25] Iyad S. Saidi, Steven L. Jacques, and Frank K. Tittel. Mie and rayleigh modeling of visible-light scattering in neonatal skin. *Appl. Opt.*, 34(31): 7410–7418, Nov 1995. doi: 10.1364/AO.34.007410. URL `http://ao.osa.org/abstract.cfm?URI=ao-34-31-7410`.

[26] George Zonios, Julie Bykowski, and Nikiforos Kollias. Skin melanin, hemoglobin, and light scattering properties can be quantitatively assessed in vivo using diffuse reflectance spectroscopy. *Journal of Investigative Dermatology*, 117(6):1452 – 1457, 2001. ISSN 0022-202X. doi: http://dx.doi.org/10.1046/j.0022-202x.2001.01577.x. URL `http://www.sciencedirect.com/science/article/pii/S0022202X15414836`.

[27] M. J. C. Van Gemert, S. L. Jacques, H. J. C. M. Sterenborg, and W. M. Star. Skin optics. *IEEE Transactions on Biomedical Engineering*, 36(12):1146–1154, Dec 1989. ISSN 0018-9294. doi: 10.1109/10.42108. URL `http://ieeexplore.ieee.org/stamp/stamp.jsp?tp=&arnumber=42108`.

[28] Richard C. Haskell, Lars O. Svaasand, Tsong-Tseh Tsay, Ti-Chen Feng, Bruce J. Tromberg, and Matthew S. McAdams. Boundary conditions for the diffusion equation in radiative transfer. *J. Opt. Soc. Am. A*, 11(10): 2727–2741, Oct 1994. doi: 10.1364/JOSAA.11.002727. URL `http://josaa.osa.org/abstract.cfm?URI=josaa-11-10-2727`.

[29] *MeVis-C 1.6/35*, 2011.

[30] *RefractiveIndex.info*, 2017. `http://refractiveindex.info/?shelf=main&book=TeO2&page=Uchida-o`[Accessed:2017-01-21].

[31] C. Stedham, M. Drapera, J. Warda, E. Wachmanc, and Pannelld C. A novel acousto-optic tunable filter for use in hyperspectral imaging systems. *Proc. of SPIE*, 6889, 2008.

[32] *Octal Channel AOTF Controller Integration Guide*, revision 1.1 edition, 2010.

[33] *Software Guide*, v3.12 edition, 2016.

[34] Macbeth color checker chart, 2017. `http://www.arrirentalstore.com/product_p/102032.htm[Accessed:2017-01-30]`.

[35] Dof 5-15 depth of field target, 2017. `http://www.edmundoptics.com/test-targets/image-analysis-test-targets/dof-5-15-depth-of-field-target/1485/[Accessed:2017-01-30]`.

[36] Diffuse reflectance grid distortion targets, 2017. `http://www.edmundoptics.com/test-targets/distortion-test-targets/diffuse-reflectance-grid-distortion-targets/3046/[Accessed:2017-01-30]`.

[37] Usaf 1951 3-bar resolving power test chart, 2017. `http://www.efg2.com/Lab/ImageProcessing/TestTargets/[Accessed:2017-01-30]`.

[38] Lise L. Randeberg. *Diagnostic applications of diffuse reflectance spectroscopy*. Doctoral thesis, Norwegian University of Science and Technology, 2005.

[39] Stig Viste. *Registration in hyperspectral and multispectral imaging*. Master thesis, Norwegian University of Science and Technology, 2017.

[40] About applying to rec, 2017. `https://helseforskning.etikkom.no/frister/soknadsfrister?p_dim=34667[Accessed:2017-01-24]`.

[41] Lise L. Randeberg, Julio Hernandez-Palacios, Mila Lilleeng, Lill Tove Nilsen, and Anne-Lene Krogstad. Uv doses and skin effects during psoriasis climate therapy, 2011. URL `http://dx.doi.org/10.1117/12.874067`.